The rheology and microstructure of branched micelles under shear

Michelle A. Calabrese, Simon A. Rogers,[1] Ryan P. Murphy, and Norman J. Wagner

Center for Neutron Science, Department of Chemical and Biomolecular Engineering,
University of Delaware, Newark, Delaware 19716

Synopsis

The rheology and shear-induced structures of a series of self-assembled surfactant worm-like micelles (WLMs) with varying levels of branching are measured using rheo- and flow-small angle neutron scattering (SANS). The degree of branching in the mixed cationic/anionic surfactant (CTAT/SDBS) WLMs is controlled via the addition of the hydrotropic salt sodium tosylate and verified by cryo-TEM. The linear viscoelasticity of the low salt (linear) micellar solutions is well-described as an extended Maxwell (Oldroyd-B) fluid, and samples exhibit shear banding under steady-shear flow. The linear viscoelasticity of more highly branched solutions deviates from Maxwellian behavior, where the plateau in G' gradually increases in slope with increasing salt content. The higher salt solutions exhibit a shear thinning regime, followed by a shear thickening regime at high shear rates. Micelle segmental alignment in the flow-gradient plane is a non-monotonic function of salt level and radial position. Spatially-resolved measurements of the segmental alignment corroborate shear banding in the linear WLMs, and the absence of shear banding with branching. Rheo-SANS measurements show that the onset of shear thickening at high rates corresponds to a structural transition. The results of this study link micellar microstructure and topology to the measured shear rheology of WLM solutions.

I. INTRODUCTION

Worm-like micelles (WLMs) are commonly used as a model system for studying polymers and polyelectrolytes [Magid (1998), Candau and Oda (2001)], and are of particular scientific interest due to their ability to self-assemble, break and reform under shear, and shear band [Spenley *et al.* (1993), Cates and Fielding (2006), Helgeson *et al.* (2009a)]. WLMs are ubiquitous in applications ranging from consumer products, cosmetics, and pharmaceuticals to industrial materials such as oil field fluids and drag reduction agents [Zakin *et al.* (1998), Yang (2002), Maitland (2000), Rogers *et al.* (2014)]. The tunable self-assembly of these “living” surfactant solutions enables a wide variety of solution morphologies and rheological characteristics that can be tailored for such applications. The linear rheology of WLMs is often well-described by an extended Maxwell (Oldroyd-B) model, where the structure breakage and reformation is significantly faster than reptation [Granek and Cates (1992), Cates and Candau (1990)] such that there is a single relaxation time. By altering the solution composition or temperature, a maximum in the zero-shear viscosity, η_0, is often observed, which has been shown to correspond to changes in the micellar topology. The increase in viscosity with added surfactant or salt results from micellar growth and entanglement. In contrast, micellar branching has been shown to lower η_0 [Candau and Oda (2001), Schubert *et al.* (2003), Ziserman *et al.* (2009), Sachsenheimer *et al.* (2014)], by providing another mechanism for stress relaxation. Unlike in polymers, micellar branch points are fluid and branches slide along a contour, thereby relieving stress. The presence of branches reduces the stress-carrying portion of the micelle to the sections between branch points. The effective micellar length is thus decreased by inducing branching, which leads to decreased viscosities [Candau and Oda (2001), Schubert *et al.* (2003), Lequeux (1992)]. As branching increases, large deviations from Maxwellian behavior are observed [Angelico

---

[1] Corresponding Author: rogers.simon@gmail.com

et al. (2012), Palazzo (2013), Koshy *et al.* (2011)]. Further increases in salt concentration lead to network condensation [Liberatore *et al.* (2009), Thareja *et al.* (2011)].

In addition to serving as a model system that can aid future studies of branched polymers, branched WLMs are of particular scientific and industrial interest due to their tunable, highly non-Newtonian flow properties. Linear WLMs tend to exhibit shear banding, a phenomenon where the flow exhibits spatial heterogeneities such that the material separates into regions of high velocity (low viscosity) and low velocity (high viscosity). Branched WLMs have shown the potential to eliminate the shear banding flow instability, which is suggested by the mitigation of the stress plateau along the flow curve [Rogers *et al.* (2014), Khatory *et al.* (1993), Berret *et al.* (1993), Lu *et al.* (2011)]. We note, however, that shear banding has been shown to be possible in models of entangled polymers that exhibit monotonic flow curves [Adams and Olmsted (2009)], such that the mechanism by which branching may or may not suppress shear banding is still under investigation. While shear thinning is optimal for injectable fracking and carrier fluids [Barati and Liang (2014)], shear banding is seemingly detrimental as fluid components may stratify or phase separate [Drye and Cates (1992), Schubert *et al.* (2004)].

While branching is widely accepted as an explanation of nonmonotonic zero-shear viscosity trends, there has been limited experimental evidence to corroborate this theory. Cryo-TEM is the most commonly used method, which provides visual evidence of branching [Ziserman *et al.* (2009), González and Kaler (2005), Kuperkar *et al.* (2008), Shrestha *et al.* (2011)]. However, this method is limited to dilute solutions and is difficult to use in studies of WLMs due to the elastic nature and high viscosities of the solutions. The blotting procedure performed while preparing cryo-TEM grids may also enforce aligned structures, and the organic nature of the materials leads to poor image quality, making quantifying information from the images difficult. PGSE-NMR diffusion measurements have been successfully used to confirm the presence of branching in reverse micellar solutions of lecithin and oil [Angelico *et al.* (2012), Palazzo (2013)], with deviations from Maxwellian behavior observed at high frequencies. Koshy *et al.* (2011) noted differences in the scaling laws for Maxwell fluids [Granek and Cates (1992), Cates and Candau (1990)] past the viscosity maximum in solutions of catanionic CTAB-NaOL. As the observed scaling of the plateau modulus, G_{N}^{0}, was stronger at lower surfactant concentrations than at higher values where branching was proposed, it was concluded that G_{N}^{0} of branched systems has a weaker dependence on surfactant concentration than linear worm-like solutions. Oelschlaeger *et al.* (2008) used DWS optical microrheology and macroscopic mechanical rheology to investigate the underlying cause of two local maxima in the zero-shear viscosity and relaxation time in solutions of CPyCL with added NaSal. They determined that the peak at low salt concentration was a transition between linear micellar growth and micellar branching. Recently, Sachsenheimer *et al.* (2014) investigated six different WLM systems covering a broad range of surfactant concentrations and salt/surfactant ratios using capillary breakup elongational rheometry (CaBER). The filament lifetime, t_{fil}, measured from the CaBER experiments was shown to depend on the plateau modulus, G_{N}^{0}, and the breakage time, τ_{break}, obtained from small-amplitude oscillatory shear rheology parameters by the scaling law $t_{\mathrm{fil}}/G_{\mathrm{N}}^{0} \propto \tau_{\mathrm{break}}^{2/3}$. Furthermore, it was shown that the filament lifetime depends more strongly on the zero-shear viscosity in the case of linear micelles than in the branched regime, suggesting that CaBER can be used to distinguish micellar topology. Scattering techniques have also been developed for the determination of branching [Burchard (1999)]; however, it is generally accepted that static scattering can detect micellar growth but is insufficient to determine branching [Koshy *et al.* (2011), Kuperkar *et al.* (2008), Shrestha *et al.* (2011), Walker (2009)]. These, and related methods, are reviewed by Rogers *et al.* (2014).

To investigate the effects of micellar branching on the steady-shear flow properties and possible shear banding instabilities, we propose a combination of nonlinear rheology and neutron scattering techniques (flow-SANS) with spatial and temporal resolution to determine the microstructural transitions that affect the macroscopic flow behavior [Eberle and Porcar (2012)]. Here, we explore the relationship between branching, microstructure, and nonlinear responses under steady shear flows using a model WLM system, where the phase behavior and microstructural length scales were systematically characterized by Schubert *et al.* (2003). The system is composed of mixed cationic and anionic surfactants cetyltrimethylammonium tosylate (CTAT) and sodium dodecyl benzene sulfonate (SDBS) near the overlap concentration ($C^{*} \approx C_{D}$=1.5% wt) and branching is induced by the addition of the hydrotropic salt sodium tosylate (NaTos). In addition to flow-SANS measurements in two of the three deformation planes, cryo-TEM and shear rheological measurements are used to provide a comprehensive analysis of the effect of added salt on the structure and flow properties of WLMs.

II. THEORY

There are several methods of inducing branching in worm-like micellar solutions, generally via the addition of salt or oppositely charged ionic surfactants. Simple salts, such as NaCl, alter the ionic strength of solution but do not penetrate the structure of the micelles, thereby having less of an effect on the micelle topology as compared to the effect of hydrotropic salts such as NaSal or NaTos [Schubert *et al.* (2003)]. In this study, the total surfactant concentration C_D is held constant at 1.5% wt (97/3% wt CTAT/SDBS) and NaTos is added from 0 to 0.25% wt solution total. Here, C_D is approximately that of the overlap concentration, C^*, between the dilute and semi-dilute regimes, as determined by a change in the scaling laws at C_D = 1.5% wt [Schubert *et al.* (2003)]. In the present WLM system, the use of oppositely charged surfactants is sufficient to induce branching at low levels with no added salt; thus the "micellar growth" region of increasing zero-shear viscosity is already surpassed. As the first viscosity maximum is not observed and the range of salt concentrations is sufficiently small so as to avoid phase separation, the zero-shear viscosity decreases monotonically with added salt. The overall micelle contour length, L_c, is governed by the micelle scission energy, which is the difference between the endcap formation energy and the electrostatic energy of the micelle, $E_{sciss} = E_c - E_e$ [MacKintosh *et al.* (1990)]. A low scission energy favors the formation of short, cylindrical micelles, whereas high scission energies lead to the formation of longer, worm-like micelles. In solutions with no added salt, the micellar head groups are primarily of the same charge, leading to stiff cylinders with a high electrostatic energy that repel each other. The addition of NaTos increases structural flexibility by screening headgroup repulsions and inter-micelle electrostatic interactions, thus reducing the net micelle surface charge. The reduction of the electrostatic energy of the system thereby increases the scission energy. The increasing scission energy makes the formation of branch points more energetically favorable [Schubert *et al.* (2003), MacKintosh *et al.* (1990)]. The penetration of the small molecule NaTos into the micelle also increases flexibility, enabling the surfactants to more easily rearrange into junctions needed to form branches as opposed to conventional convex endcaps.

Granek and Cates (1992) and Cates and Candau (1990) describe the stress relaxation of linear worm-like micelles by a combination of reptation, breakage, and reformation dynamics. While strictly applicable to *nonionic* systems, the theory and scaling laws agree reasonably with experimentally-measured values when applied to the ionic, linear systems in this work. In the fast-breaking limit, the time required for a micelle to reptate out of its tube is much greater than the breakage time, so that any linear chain undergoes many breakage and recombination events before reptation processes alone could relax the entirety of the material stress. Linear worm-like micelles in the fast-breaking limit are therefore well described by a simple Maxwell model with a single relaxation time, τ_R [Granek and Cates (1992), Cates and Candau (1990)]. The relaxation time for a Maxwell fluid is related to the breakage and reptation times ($\tau_{\text{reptation}}, \tau_{\text{break}}$) via $\tau_R = (\tau_{\text{break}}\tau_{\text{reptation}})^{1/2}$ [Cates and Candau (1990)]. Small amplitude oscillatory shear measurements are often used to determine τ_R, which in a Maxwell framework is defined as the timescale (inverse of the angular frequency) at which the dynamic moduli are equal. At the crossover frequency ω_c, $G'(\omega_c) = G''(\omega_c)$ and $\tau_R = 1/\omega_c$. A parametric representation of the linear viscoelastic (LVE) data, often referred to as a Cole-Cole plot, where G'' is plotted against G', is perfectly semicircular for a Maxwell fluid. In linear WLMs, the experimental data shows excellent agreement with the Maxwell model at low frequencies. However, as the angular frequency increases, deviations from the model, including a local minimum in G'', are observed due to Rouse modes [Granek and Cates (1992)]. The frequency at which G'' exhibits a local minimum, ω_{min}, gives an estimate of the breakage time ($\omega_{min} \approx 1/\tau_{break}$) and can be related back to the contour and entanglement lengths for linear, nonionic micelles (l_e and L_c, respectively) by $G''_{min}/G'_\infty \approx l_e/L_c$ [Granek and Cates (1992), Granek (1994)]. From the theory of rubber elasticity, the entanglement length is related to the mesh size, ξ_M, by $l_e \approx \xi_M^{5/3}/l_p^{2/3}$ [de Gennes (1979), Doi and Edwards (1986)]. The mesh size can then also be estimated by $\xi_m \approx (k_BT/G_{\text{N}}^0)^{1/3}$ [de Gennes (1979), Doi and Edwards

(1986)]. The extended Maxwell or Oldroyd-B model, where G'' is augmented with a high shear rate viscosity ($G'' = G''_{Maxwell} + \eta_{\infty}\omega$), satisfactorily captures this high frequency behavior.

Notably, the more charged or branched the system, the higher the expected deviation from such scaling laws. Lequeux (1992) extended the results of Cates to interconnected networks of micelles, in which branch points move fluidly along a contour and act as another mechanism for stress relaxation unlike in chemically-bonded polymers. As branch points form, the length scales defined for linear micelles, such as the entanglement length, become ill-defined. The effective micelle length becomes the distance between branch points, leading to a decreased zero-shear viscosity. Consequently, the sliding branch points decrease the reptation time, τ_{rep}, and therefore the material relaxation time, τ_R. In linear WLMs in the fast breaking limit, breakage and reformation dynamics lead to a single relaxation time, which is manifested as a semi-circle in the Cole-Cole representation. However, LVE data from polymeric systems, where breakage and reformation are not available mechanisms for stress relaxation, are almost never semicircular in the Cole-Cole representation. While both systems have inherent polydispersities in the average chain length, the chemically-bonded nature of the polymer requires reptation of the full chain for complete stress relaxation, whereas the living nature of the micelles leads to a single effective chain length. Polymeric branching also leads to significant deviations from Maxwellian behavior [Hatzikiriakos (2000)] and increases in viscosity because the branch points are not mobile as they are for WLMs. Similar trends have been observed in micellar solutions with high salt concentrations and branching [Khatory *et al.* (1993), Berret *et al.* (1993), Lu *et al.* (2011)], with anomalous behavior at high frequencies. Therefore, as branching increases and more mechanisms of relaxation become available, the LVE rheology increasingly deviates from Maxwellian behavior.

III. MATERIALS AND METHODS

A. Materials

The WLM system presented was previously well-characterized over a range of added salt concentrations [Schubert *et al.* (2003)]. The WLM solutions are composed of mixed cationic and anionic surfactants CTAT and SDBS with a total surfactant concentration held constant at 1.5% wt (97/3 weight ratio of CTAT/SDBS; 35.8 mM CTAT/1.45 mM SDBS). Sodium tosylate (NaTos) was added as a hydrotropic salt to induce structural changes, ranging from 0.0% wt NaTos to 0.25% wt NaTos. Sodium tosylate and CTAT were obtained from Sigma-Aldrich. CTAT was recrystallized twice from a 50/50 mixture of ethanol and acetone. Sodium tosylate was used as received. Soft-type (linear chain) SDBS was obtained from TCI and used as received. All surfactant solutions were prepared at room temperature in D_2O (Cambridge Isotopes, 99.8%) that was filtered before use. All samples were incubated in a 35 °C water bath for 3 days before performing SANS or rheological measurements to ensure chemical, kinetic, and thermal stability.

B. Cryo-TEM

Cryo-TEM imaging was performed on a Technai G2 12 Twin TEM operating at 120 kV. Samples were prepared using an FEI Vitrobot at 35 °C and 100% relative humidity. Prior to sample preparation, the TEM grids (Quantifoil R 2/1 or lacey carbon) were plasma cleaned for 60 s. A 3 μl volume of each sample solution was pipetted onto the grid inside the sample chamber. Using an automated system, each sample was blotted twice to remove excess sample prior to vitrification in liquid ethane. The blotting conditions were consistent for each sample: 3 s blot time, 5 s wait time, 10 s drain time, and 0 blot force. The grids were transferred into liquid nitrogen for storage before imaging. Images were recorded using a Gatan CCD camera and were imaged at a nominal underfocus to enhance phase contrast. The temperature of the probe was maintained between -178 and -180 °C during imaging.

C. Rheometry

The main rheology experiments were performed on a 0.01% wt NaTos solution (low salt) and a 0.10% wt NaTos solution (high salt) with supplementary experiments performed on other salt concentrations. All rheometry measurements were performed at 35 °C ± 0.1 °C. Reported rheological tests were performed on an ARES G2 strain-controlled rheometer (TA Instruments, New Castle, DE) with temperature control from a ThermoCube circulating chiller (AMS Technologies). A concentric-cylinder Couette geometry was used with a stationary inner cylinder, stainless steel DIN bob (R_1 = 13.84 mm) and a rotating outer cylindrical cup (R_2 = 15.00 mm), such that the gap width, H, was 1.16 mm. The position within the gap is notated as r/H. Using the length of the Couette bob, L, the resulting aspect ratio, Γ = L/H, was 35 and the gap to radius ratio, ε = H/R_1, was 0.084. Select rheological measurements were repeated on an Anton-Paar MCR-501 stress-controlled rheometer operating in strain-controlled mode. Two separate concentric-cylinder Couette geometries were used, both with a moving inner cylinder and stationary outer cup and a solvent trap filled with D_2O to provide a saturated atmosphere. In the first configuration R_1 = 24.0 mm and R_2 = 25.0 mm, resulting in ε = 0.042 and Γ = 36. In the second configuration R_1 = 13.5 mm and R_2 = 14.5 mm, such that ε = 0.074 and Γ = 36. Rheology was verified to be independent of instrument and geometry.

Samples were conditioned in the rheometer for 10 minutes at 35 °C to achieve thermal equilibrium. Frequency sweeps were then performed using a strain amplitude of 5% to measure the linear viscoelastic response of each sample. The delay time between measurements was at least 10 times that of the material relaxation time, determined by the crossover frequency (τ_R= $1/\omega_c$). Initial sweeps were performed in triplicate over the course of one hour to ensure structural and thermal equilibrium after loading. Sweeps were performed over a frequency range of ω = 0.01 to 25 rad $\cdot$ s^{-1} (increasing and decreasing) for the sample with low salt (0.01% wt NaTos) and from ω = 0.1 to 25 rad $\cdot$ s^{-1} (increasing and decreasing) for the sample with high salt (0.10% wt NaTos). Hysteresis was not observed using this protocol. Amplitude sweeps were performed at the frequency limits to verify that the dynamic moduli are independent of strain amplitude at 5%. Corroborative frequency sweeps were performed at several strain amplitudes (5% to 20%) and using correlation and waveform analysis.

Steady shear flow sweeps were performed on both samples to measure the steady-state material viscosity and stress over a range of shear rates (0.01 - 575 s^{-1}). Sweeps were performed in the increasing and decreasing directions with at least $10\tau_R$ of rest time between each datum without observable hysteresis. The flow curves were verified to be those of the steady-state with long-time (300 - 1800 s) stress and viscosity measurements from peak hold tests. To examine the stability of the flow near the shear thickening regime observed at high rates, additional startup measurements were performed in both the ARES and MCR rheometers for 1200 - 1800 s on the high salt sample (0.10% wt NaTos). In both geometries, the stress fluctuations were 3.5% or less at steady state ($t > 10$ s). These results are detailed further in the Supporting Information. Frequency sweeps were also performed after each rheological test to confirm the absence of foaming, evaporation, or irreversible changes from shear.

D. Static SANS measurements

Static SANS measurements were taken at the National Institute of Standards and Technology (NIST) Center for Neutron Research in Gaithersburg, MD on the NG-7 30 m SANS instrument [Porcar *et al.* (2011)]. Samples were measured in 2 mm quartz cells with temperature control set to 35 °C ± 0.1 °C to prevent crystallization of the material. The measured scattering vector, q, ranged from 0.001 Å^{-1} to 0.5 Å^{-1} using detector distances of 15.3 m (lens), 4 m and 1 m. The neutron wavelength, λ, was 6 Å for the 4 m and 1 m configurations, and 8.4 Å for the 15.3m with lens configuration. The wavelength spread, $\Delta\lambda/\lambda$, was 11.5% for both wavelengths. Raw data was reduced to an absolute scale as outlined by NIST standards by accounting for background, empty cell scattering, and detector efficiency [Kline (2006)]. Absolute scattering profiles were shown to be independent of instrument and sample environment from additional static SANS experiments at NIST and on the D-22 instrument at the Institut Laue-Langevin (ILL) in Grenoble, France. Measurements from six additional configurations showed excellent agreement (see Supporting Information): NG-7 with Anton-Paar MCR501 rheometer, NG-7 with 1-2 shear cell, NG-3 30 m SANS with 2 mm quartz cells, NG-3 with rheometer, NGB-30 with rheometer, NGB-10 with rheometer, and D-22 (ILL) with 1-2 shear cell.

E. Rheo-SANS measurements in the 1-3 (flow-vorticity) plane

Rheo-SANS experiments in the 1-3 (flow-vorticity) plane were conducted at the NIST Center for Neutron Research on the NGB 30m SANS instrument. An Anton-Paar MCR-501 stress-controlled rheometer (used in strain-controlled mode) with a concentric-cylinder Couette geometry was used for all experiments. The rheometrical geometry was composed of a titanium moving inner cylinder and stationary outer cup as previously stated (R_1= 24.0 mm; R_2 = 25.0 mm; Γ = 36; ε = 0.042). A solvent trap filled with D_2O was utilized to provide a saturated atmosphere and to limit sample evaporation. The neutron wavelength, λ, was 6 Å with a wavelength spread $\Delta\lambda/\lambda$ = 13.1%. Two detector distances (8 m, 1.65 m) were used to cover a q-vector ranging from 0.006 Å^{-1} to 0.2 Å^{-1}. Results were corroborated with select rheo-SANS experiments on the NG-3 instrument using a Couette geometry with a 0.5 mm gap (R_1= 13.5 mm; R_2 = 14.0 mm; Γ = 36; ε = 0.042) and on the NGB-10 instrument using a Couette geometry with a 1.0 mm gap (R_1= 13.5 mm; R_2 = 14.5 mm; Γ = 36; ε = 0.042).

Two vertically-oriented beam apertures were placed prior to the rheometer to minimize spatial smearing that results from the rheometer curvature. The apertures limit the scattering volume to a small region where the flow direction, beam direction, and slit orientation are mutually orthogonal, with the beam and flow directions spanning the horizontal plane. A 5 mm x 20 mm source aperture was positioned at the end of the neutron guides. A sample aperture (2 mm x 20 mm slit) was centered approximately 3 inches prior to the quartz windows of the rheometer. Select experiments were repeated with a 3 mm x 20 mm source aperture and no significant resolution effects were observed.

F. Flow-SANS measurements in the 1-2 (flow-gradient) plane

Flow-SANS experiments in the 1-2 (flow-gradient) plane of shear were conducted at both the NIST Center for Neutron Research and the Institut Laue-Langevin. All experiments were performed in a short gap Couette cell (5mm path length) as previously described [Liberatore *et al.* (2006), Gurnon *et al.* (2014)]. The shear cell consists of a rotating inner cylinder (R_1 = 25.5 mm) and an outer stationary cylinder (R_2 = 26.5 mm) such that the gap width is 1.0 mm, Γ = 5 and ε = 0.039. Temperature control is maintained by using a flow-through port within the cell that is connected to a heated water bath (35 °C ± 0.1 °C for all experiments). Two cadmium beam slits are placed prior to the front wall of the shear cell. The first is a 5 mm slit oriented horizontally which constrains the measured region to one where the flow is essentially vertical. The second slit is oriented vertically, and has a width based on desired spatial resolution. A stepper motor is used to translate the slit across the gap, providing spatial resolution. The motor is calibrated by taking empty cell transmission measurements across the cell gap. The edges of the gap are identified by the large changes in the number of transmitted neutrons from the aluminum to the fluid (air) in the empty cell [Liberatore *et al.* (2006), Gurnon *et al.* (2014)].

Steady-shear experiments were performed over a range of shear rates. Empty cell and sample transmission measurements were taken at each spatial position across the gap. Samples were allowed to equilibrate for a minimum of 30 minutes after loading, and multiple static measurements were taken during the equilibration period to identify any structural changes. Any bubbles were removed from the cell before the start of each experiment. Static structure measurements were taken at the end of every five steady-shear experiments to ensure that the sample had not been subjected to bubbling, evaporation, or irreversible changes from shear. Data was reduced to an absolute scale as outlined by NIST standards [Kline (2006)].

The primary flow-SANS experiments were performed at NIST using the NG-7 30m SANS instrument. All NIST experiments were performed with a 0.1 x 3 mm straight secondary beam slit. Measurements were taken at several positions across the gap, ranging from r/H = 0.1 to r/H = 0.9. The main experiments were performed using an aluminum shear cell with magnetic coupling, with one aluminum window and one quartz window to view the sample. Steady-shear scattering experiments were performed with a detector distance of 8 m and 6 Å neutrons for a minimum of one hour. The measured scattering vector, q, ranged from 0.005 Å^{-1} to 0.05 Å^{-1}

with $\Delta\lambda/\lambda$ = 11.5%. Complimentary steady-shear experiments were conducted in a titanium shear cell for a minimum duration of one hour at a detector distance of 8 m with 6 Å neutrons and a wavelength spread of $\Delta\lambda/\lambda$ = 11.5%. The q-range in those experiment covered the range 0.007 Å^{-1} to 0.05 Å^{-1}.

Select experiments on the sample with low salt (0.01% wt NaTos) were performed on the D-22 SANS instrument at ILL. Experiments were performed at a detector distance of 11.2 m with 6 Å neutrons and a wavelength spread of $\Delta\lambda/\lambda$ = 10%. A 0.3 mm wide curved slit was used for these experiments. Experiments were performed at two positions located near the inner (r/H = 0.3) and outer wall (r/H = 0.7) of the shear cell. Steady-shear experiments were conducted for 10 minutes covering a q-range of 0.0044 Å^{-1} to 0.065 Å^{-1}. Repeated experiments at a detector distance of 17.6 m yielded identical results within error, indicating that the decrease in resolution from 17.6 m to 11.2 m was insignificant.

IV. RESULTS

Results are presented from micellar solutions with different salt content, ranging from 0.0% wt NaTos to 0.25% wt NaTos. In order to remove micellar growth and shape as confounding variables when determining the effects of added salt, all samples studied are at surfactant and salt concentrations past the commonly observed viscosity maximum. Here, the micelles are truly "worm-like," where the persistence and contour lengths are well-separated ($l_p << L_c$), thus removing effects that may be attributed to the shape and length of shorter, rodlike micelles. To verify the expected structure of the micelles, cryo-TEM, static SANS, and linear viscoelastic (LVE) regime rheology measurements were performed. These structural results and the linear viscoelastic rheology were favorably compared with the results of Schubert *et al.* (2003). Following the structure confirmation and LVE rheology, the effect of added salt on the rheology and flow-induced structure of the micelles was examined. These results are restricted to a direct comparison of two samples from two salt regimes of interest: 0.01% wt NaTos (referred to as low salt) and 0.10% wt NaTos (high salt).

A. Structure Confirmation

1. Cryo-TEM

Cryo-TEM was performed on solutions with a fixed surfactant concentration (C_D = 1.5% wt) and various salt concentrations to visualize the effect of salt concentration on the structure: low (0.01% wt NaTos), high (0.10% wt NaTos), and very high salt (0.15% wt NaTos). Here, the surfactant concentration lies on the boundary of the dilute and semi-dilute regimes ($C_D = C^* \approx$ 1.5% wt), as noted by a change in the micellar scaling laws at this concentration [Schubert *et al.* (2003)]. As opposed to inducing structural changes such as branching by changing the surfactant concentration, the structure of these solutions is controlled by a change in the concentration of added salt. A qualitative distinction between the resulting structures is observed in Figure 1, where the 0.01% wt NaTos (a, red) and 0.10% wt NaTos (b, blue) worm-like micelles are compared. Additional images of these two solutions, along with images of the 0.15% wt NaTos solution, can be seen in the Supporting Information.

Figure 1a (red) shows the 0.01% wt NaTos solution containing linear micelles and no observable branch points. In contrast, the 0.10% wt NaTos solution shown in Figure 1b (blue) shows a high probability of finding a branch point along a contour, and contains a variety of loops and branch points. While the concentration makes it difficult to differentiate between branch points and overlapping micelles, the white arrows point to clear loops or three-fold junctions where overlap does not occur. These junctions and other irregular structures are also observed in the very high salt (0.15% wt NaTos) solution (Supporting Information), and become more prevalent with the addition of the hydrotropic salt. The structures are consistently observed across multiple images from different grid locations. These results are consistent with the findings of Schubert *et al.* (2003), where branching was proposed with increasing hydrotropic salt content. While all samples undergo the same preparation and imaging conditions, flow-aligned structures are observed in the linear system (0.01% wt NaTos) that are absent in the samples of higher salt content. This alignment is difficult to avoid and is enforced by the micellar topologies: the linear structures align more easily than those containing branch points or network-like structures that introduce steric effects.

The insets show the larger-scale structural differences, where long thread-like micelles (a) and interconnected structures (b) are observed. The micellar diameter, d_{cs}, was estimated to be between 40 Å and 50 Å for all samples using ImageJ analysis on multiple images. Micellar diameter was not a function of salt concentration within the precision obtainable by cryo-TEM. The diameter measurements agreed with the cross-sectional radius of 21.4 Å (d_{cs} = 42.8 Å) determined by Schubert *et al.* (2003) via static SANS. Additionally, Schubert *et al.* (2003) calculated the contour length of the micelles to be on the order of several microns, which was supported with additional cryo-TEM images. Qualitatively, the number of branch points is much higher in the 0.10% wt NaTos sample (and 0.15% wt NaTos sample) than in the 0.01% wt NaTos sample. Although these and additional images in the Supporting Information show the formation of branch points with added NaTos, due to the limited contrast and the tendency of the samples to shear align with the cryo-TEM grid, no quantitative relationships between NaTos content and structure have been developed.

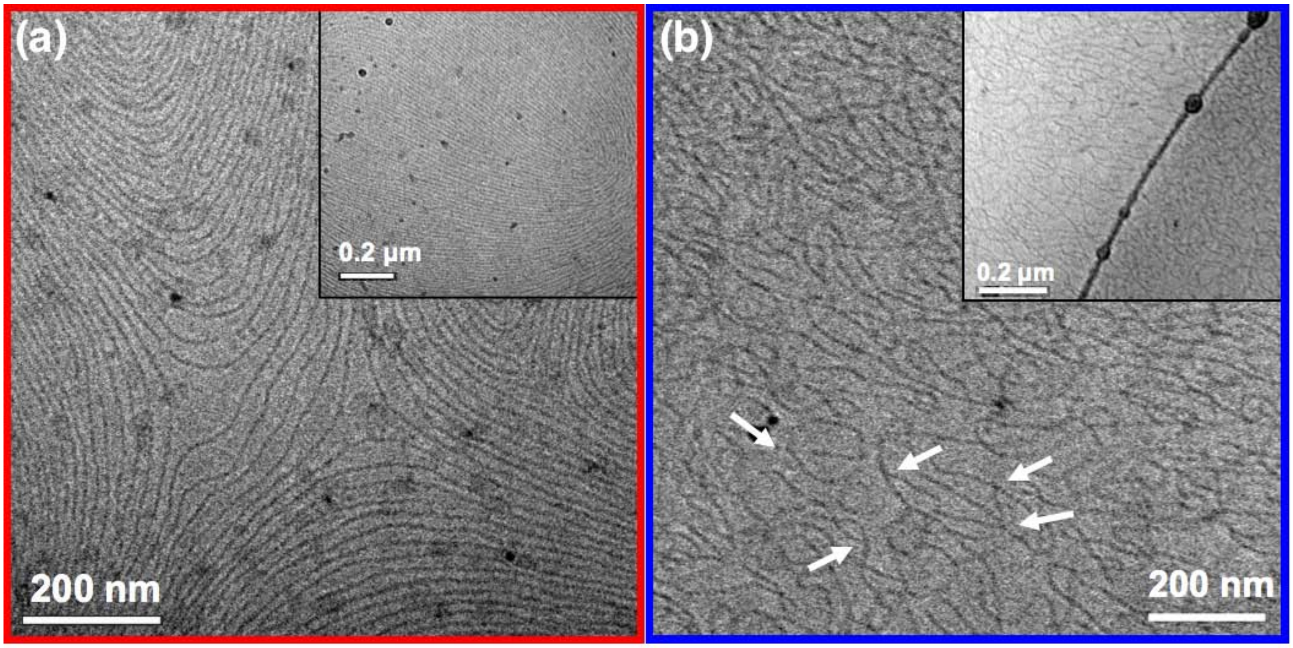

Figure 1: Comparison between CTAT/SDBS worm-like micellar solutions with a fixed surfactant concentration ($C^* \approx C_D$=1.5% wt) with low salt (a, 0.01% wt NaTos, red) and high salt (b, 0.10% wt NaTos, blue). (a) Chains are highly linear. The inset provides a larger scale view of the long, linear structures apparent throughout the sample. (b) Micelles have identifiable branch points and form a variety of junctions, loops, and other structures. The inset shows the larger scale morphology that contrasts the linear micelles observed in the (a) inset.

2. SANS

Static small angle neutron scattering measurements were performed to determine the equilibrium structures and micellar length scales of the WLMs with varying salt content [Schubert *et al.* (2003)]. SANS results were used to calculate the micellar radius using several models, which was then quantitatively compared to the cryo-TEM estimates and the length scales determined by Schubert *et al.* (2003). Figure 2 shows the 1-D azimuthally-averaged SANS measurements in the full q-range from 0.001 Å^{-1} to 0.5 Å^{-1} corresponding to real space dimensions on the order of 10 Å to 6000 Å. A 2-D isotropic scattering pattern for the low salt system (0.01% NaTos, red) and high salt system (0.10% NaTos, blue) are shown to highlight the differences in the scattering between the two samples. In the low salt system, there is a strong interaction peak that appears in the 2-D pattern as an intensity ring at q = 0.022 Å^{-1}. In real space, this q-value corresponds to a distance on the order of 300 Å, which is indicative of the preferred inter-micellar separation distance arising from the electrostatic repulsions between micellar segments. As the intensity is isotropic, the sample is also isotropic with no net alignment of the micellar segments. With increasing salt concentration, the electrostatic interactions are progressively screened and the interaction peak is dampened. In the 2-D scattering of the 0.10% wt NaTos system, the mitigation of the interaction peak is evident, as the ring structure is no longer visible.

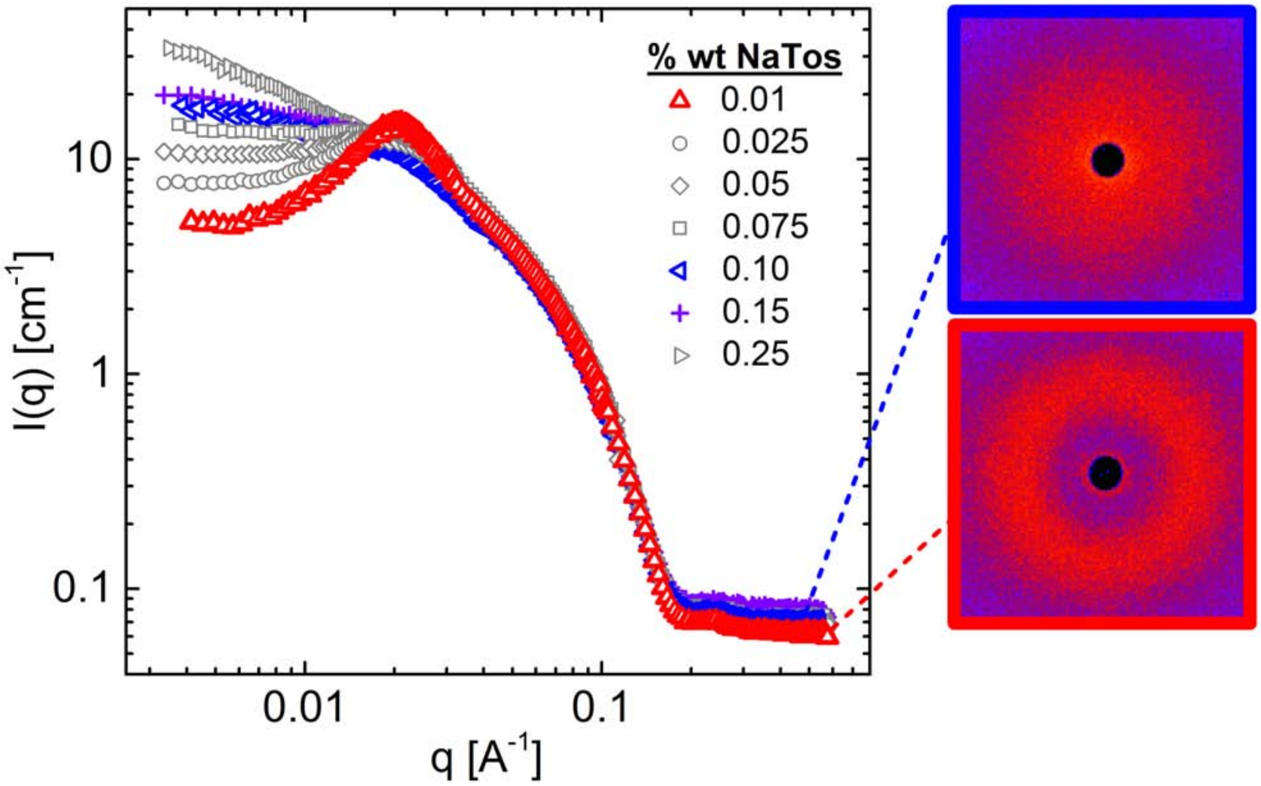

Figure 2: 1-D azimuthally-averaged static SANS for CTAT/SDBS WLM solutions with a range of salt (0.01% wt NaTos) to (0.25% wt NaTos). 2-D scattering patterns are highlighted for the low salt (0.01% wt NaTos, red) and high salt system (0.10% wt NaTos, blue). The strong interaction peak at low salt concentration manifests itself as a ring in the 2-D scattering pattern (red), whereas the electrostatic interactions are screened at high salt concentrations (blue), leading to the disappearance of the interaction peak. The 0.15% wt NaTos 1-D scattering is also shown (purple) to highlight the structural similarities between the 0.15% wt and 0.10% wt sample, in qualitative agreement with the cryo-TEM results.

The 1-D scattering of the 0.15% wt NaTos solution is also highlighted (purple + symbol) to show the structural similarities between this sample and the 0.10% wt NaTos solution. The similarity in the SANS between these two samples is supported by the cryo-TEM results which show comparable features (see Supporting Information). At the maximum salt concentration shown in Figure 2 (C_s = 0.25% wt), the interaction peak has completely disappeared. The high-q scattering ($q \geq 0.04$ Å^{-1}) for all samples collapses onto one curve, indicating that the basic cylindrical structure of the micelles does not change with salt concentration. To determine micellar length scales, scattering models for a cylinder and flexible cylinder were fit to the data in the high-q region beyond the influence of the interaction peak. As expected, both models yielded similar results and all cross-sectional radii, r_{cs}, ranged from 20.2 Å to 21.3 Å. Using a simpler Guinier approximation yields r_{cs} = 21.2 Å to 21.9 Å, in good agreement with the Guinier analysis of Schubert *et al.* (2003) where r_{cs} = 21.2 Å to 21.6 Å. As expected, the cross-sectional radius of the micelles slightly decreases with increasing salt concentration, due to screened repulsions that decrease the effective headgroup size.

B. The effect of hydrotropic salt on the rheology of WLMs

1. Relaxation time and zero-shear viscosity as a function of added salt

The material relaxation time, τ_R, and the zero-shear viscosity, η_0, of the WLMs over the range of added salt (0.0% wt - 0.25% wt NaTos) were examined as a function of salt concentration and the ratio of the concentrations of the ions, which self-assemble to form the micelles. SDBS and NaTos dissociate to form negatively charged ions and CTAT forms positively charged ions in solution. The material relaxation time is defined as $\tau_R = 1/\omega_c$, where ω_c is the angular frequency at which G' and G'' are equal in the linear viscoelastic regime (crossover frequency). The zero-shear viscosity and an estimate of the shear relaxation time, τ_v, were determined by fitting the Cross Model (Equation 1) [Cross (1965)]:

$$\eta(\dot{\gamma}) = \eta_\infty + \frac{\eta_0 - \eta_\infty}{1+(\dot{\gamma}\tau_v)^m} \tag{1}$$

where η_∞ is the high shear viscosity and the exponent m = N + 1 and ranges between 1.0 and 1.7, where N is the power law index.

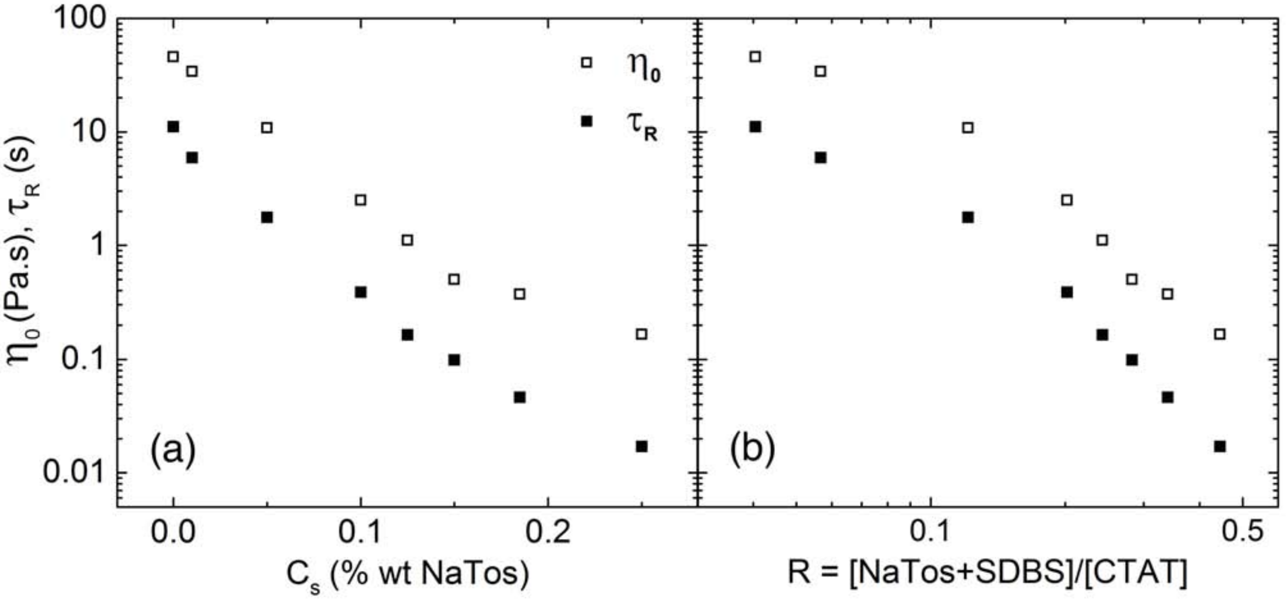

Figure 3: Zero-shear viscosity, η_0, and rheological relaxation time, τ_R, as a function of salt concentration (a) and ion concentration ratio (b). Both parameters are decreasing functions of salt and ion ratio, indicating that the system has surpassed the commonly-observed first viscosity maximum in WLM systems. The range of salt concentration is limited such that a second viscosity maximum is not observed. The associated error in both metrics determined in samples with multiple preparations is smaller than the symbol size.

For the surfactant concentration used here (C_D = 1.5% wt CTAT/SDBS in 97/3 wt ratio), Schubert *et al.* (2003) indicated that η_0 and τ_R of the micelles decrease monotonically as a function of increasing salt concentration over the range of C_s = 0 to 0.25% wt NaTos. Figure 3a confirms this trend in both η_0 and τ_R. At C_D = 1.5% wt, the micelles are very long, even at low salt concentrations, as evidenced by the cryo-TEM images. Accordingly, the commonly-observed viscosity maximum is effectively shifted to negative salt concentrations at this concentration of mixed surfactant. The viscosity maximum is only observed at lower surfactant concentrations with increasing salt concentration at the 97/3 weight ratio of CTAT/SDBS [Schubert *et al.* (2003), Koehler *et al.* (2000)]. The decreases in η_0 and τ_R with increasing ion concentration ratio scale with similar dependences, and are comparable to the viscosity and relaxation time trends reported by Sachsenheimer *et al.*

(2014) for related WLM solutions, including CTAB/NaSal (Figure 3b). The observed trends are qualitatively similar to those of the CTAB/NaSal solutions between the two observed viscosity maxima (as a function of ion concentration), which is expected given the functional and structural similarities between both surfactants and salts [Sachsenheimer *et al.* (2014)]. In the present study, a second viscosity maximum was not observed, which is likely due to the limited range of salt concentrations examined.

2. Linear viscoelastic (LVE) regime rheology as a function of added salt

The linear viscoelastic rheology of the samples (0.01% - 0.25% wt NaTos) was measured to determine characteristic differences with added salt and to estimate characteristic length and time scales. Results were compared to an extended Maxwell (Oldroyd-B) model as previously performed [Liberatore *et al.* (2009), Helgeson *et al.* (2009b)]. As seen in Figure 4a, the crossover frequency, ω_c, increases with increasing salt content. As τ_R is the inverse of the crossover frequency, τ_R of the high salt (0.10% wt NaTos) sample is an order of magnitude shorter than that of the low salt case (0.01% wt NaTos). The LVE rheology shows that the value of the moduli at the crossover point ($G_c(\omega_c)$) is not significantly affected by low levels of salt. However, G_c increases significantly at high salt content, as observed in the 0.185% and 0.25% wt NaTos samples.

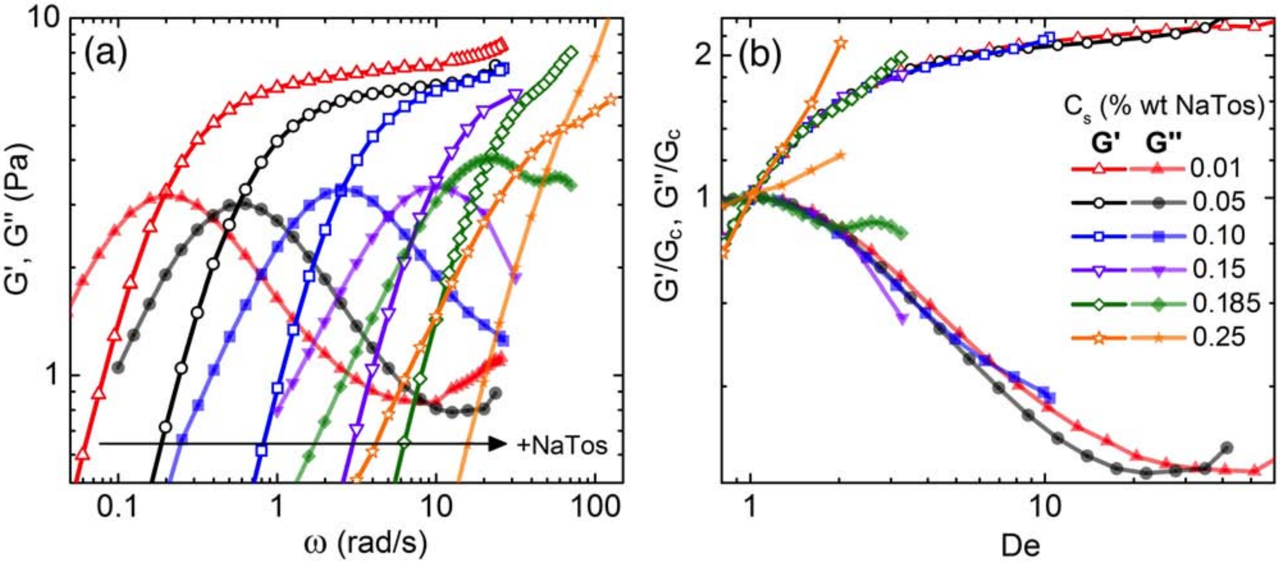

Figure 4: Dynamic moduli across the range of salt concentrations studied (0.01% wt NaTos to 0.25% wt NaTos). (a) The low salt system is a nearly perfect extended Maxwell fluid over the range of angular frequencies investigated with the exception of a slight upturn in G' in the plateau region. With increasing salt content, the upturn in G' at $\omega > \omega_c$ becomes increasingly significant, and the 0.25% wt NaTos sample has no apparent plateau over the frequency range. (b) Deviations from the extended Maxwell model with increasing salt concentration are more apparent when the moduli are normalized by the crossover modulus, G_c and compared vs. De.

The low frequency LVE for the WLMs is dominated by changes in the relaxation time due to the addition of hydrotropic salt but is otherwise qualitatively similar. As salt concentration increases, the Deborah number ($De = \omega\tau_R$) at which deviations from Maxwellian behavior occur decreases, as seen in Figure 4b, where the dynamic moduli are normalized by G_c and the frequency by ω_c. For example, the Deborah number of the G'' minimum at high frequency decreases systematically with added salt. The slope of the plateau in G' gradually increases with added salt until the G' plateau essentially disappears when $C_s \geq 0.185\%$ wt NaTos. These deviations in LVE behavior are in agreement with results from Khatory *et al.* (1993), where the deviations from Maxwellian behavior in the Cole-Cole representation of the data increase significantly as the salt concentration, and therefore correlation length, increases.

3. Steady shear rheology of 0.01% and 0.10% wt NaTos solutions

In order to compare the specific effects of added salt on the shear rheology, the steady-state viscosity and stress were compared both at equivalent shear rates (Figure 5a) and Weissenberg numbers (Figure 5b) for the 0.01% wt NaTos (low salt) and 0.10% wt NaTos (high salt) samples. Here, the Weissenberg number, Wi, is the product of the shear rate and the material relaxation time, $Wi = \tau_R \dot{\gamma}$. Figure 5 shows shear thinning behavior in both samples, where the zero-shear viscosity, like the relaxation time, decreases by an order of magnitude with an order of magnitude increase in added salt content. Results were fit by the Cross Model (Equation 1) to yield $\eta_{0,\text{low salt}}$ = 34 Pa·s and $\eta_{0,\text{high salt}}$ = 2.6 Pa·s (Table 1).

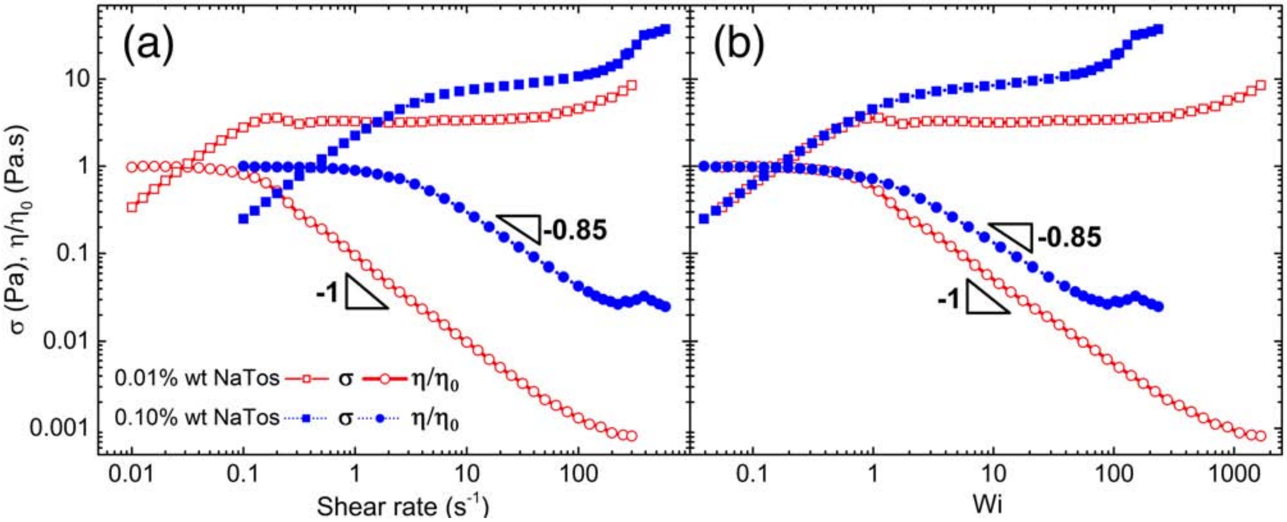

Figure 5: Steady-shear flow curve of the low (0.01% wt NaTos) and high salt (0.10% wt NaTos) solutions on an absolute scale (a) and Weissenberg number scale (b).

Figure 5 shows that while the difference in stress between the two samples is a nonmonotonic function of shear rate, the stress is always higher in the high salt case at an equivalent Wi. Ultimately, this trend in the stress is a result of the shear thinning response and how it differs in the two solutions. Whereas both samples shear thin, the degree of shear thinning is mitigated by adding salt, which can be observed by the slope in the viscosity curves of k = -1 in the low salt system (red) and k = -0.85 in the high salt system (blue). This translates to a power law index of N = 0 in the low salt sample and N = 0.15 in the high salt sample. The power law index N = 0 applies to the stress plateau in the low salt sample (red), which spans a wide range of shear rates (Wi = 1 to $Wi \approx$ 300). The stress plateau is strongly suggestive of shear banding at these shear rates. Beyond the shear banding region, the viscosity in the low salt sample begins to approach its minimum, high rate value, η_∞. In the high salt sample (blue), the stress maintains a positive slope, which covers a much smaller range of shear rates ($1 \leq Wi \leq 40$) and is indicative of a strongly shear thinning solution. At high shear rates and Weissenberg numbers, the high salt system shows reproducible shear thickening behavior. The shear thickening is highly repeatable amongst additional sample preparations and is also observed in samples with higher salt concentrations. Upon shear startup, it is well known that shear banding can take hundreds of seconds to develop in a worm-like micellar solution [Grand *et al.* (1997), Britton and Callaghan (1999), López-Barrón *et al.* (2014)]. In the low salt sample, the steady-state stress response is observed only after 50 - 100s, at minimum, for the shear rates in the stress plateau, which is consistent with shear band formation. Conversely, the steady-state stress response in the high salt solution is achieved rapidly after shear startup ($<$ 10s) for all shear rates shown, in accordance with shear thinning.

Table 1 provides a summary of the differences in the length and time scales between the two samples, determined from rheology and SANS data. Also included are estimates of length scales that can be derived

Table 1: Characteristic length and time scales of low and high salt (0.01%, 0.10% wt NaTos) WLMs

Time or length scale	**Method**	**Low salt**	**High salt**
ω_c (rad $\cdot$ s^{-1})	LVE rheology	0.18	2.6
τ_R (s)	LVE rheology	5.6	0.39
η_0 (Pa·s)	Steady shear rheology	34	2.6
η_∞ (Pa·s)	Extended Maxwell model	N/A	0.027
η_∞ (Pa·s)	Steady shear rheology	0.025	N/A
Power law index, N	Steady shear rheology	0	0.15
G_{N}^0 (Pa)	LVE rheology	7.4	7.2
G''_{min} (Pa)	LVE rheology	0.80	0.96
τ_{break} (s)	LVE rheology/scaling laws	0.13	0.03
τ_{rep} (s)	LVE rheology/scaling laws	230	4.9
r_{cs} (Å)	cryo-TEM	20 - 25	20 - 25
r_{cs} (Å)	SANS flexible cylinder model	21.3	20.4
r_{cs} (Å)	SANS, Schubert *et al.* (2003)	21.4 ± 0.2	
ξ_M (Å)	scaling laws	830	840
ξ_M (Å)	Schubert *et al.* (2003)	~900 - 1000 (in H_2O)	
l_e/L_c	scaling laws	0.091	0.133
l_e (Å)	scaling laws	730	1700
l_e (Å)	Schubert *et al.* (2003)	N/A	2050 (in H_2O)
L_c (Å)	scaling laws	8,100	13,000
L_c (Å)	Schubert *et al.* (2003)	N/A	21,000 (in H_2O)
l_p (Å)	SANS cylinder model	1000	300
l_p (Å)	rheo-optics, Schubert et al. (2003)	850 (0.05% NaTos)	310 (in H_2O)

from fits to SANS data or by micellar scaling laws [Granek and Cates (1992), Cates and Candau (1990), Granek (1994), de Gennes (1979), Doi and Edwards (1986)]. These length scales include the persistence length l_p, mesh size ξ_M, entanglement length l_e, and contour length L_c. While these scaling laws are most applicable to nonionic, linear micelles, the values are on the same order of magnitude as results from light scattering and other methods employed by Schubert *et al.* (2003), which are shown for comparison. It is to be noted that the majority of their measurements were performed in samples in water (as opposed to D_2O) as the solvent, which can result in rheological differences [Lopez-Barron and Wagner (2011)]. Interpretation of these length scales for the high salt sample is to be cautioned as the theories do not explicitly account for topological changes that may result from adding salt. While it is difficult to derive quantitative information from cryo-TEM, these predictions appear to be in line with observations from the images.

C. The effect of hydrotropic salt on the shear-induced microstructure of WLMs

1. 1-3 plane rheo-SANS

As the rheological results suggest different mechanisms of shear thinning between the low (0.01% wt NaTos) and high (0.10% wt NaTos) salt samples, structural SANS measurements were performed to compare the flow-induced structures of the micelles at equivalent absolute shear rates. Rheo-SANS measurements were taken in the 1-3 (flow-vorticity) plane at nominal shear rates along the steady shear flow curves (Figure 6). Under shear flow, micellar segments often align in the flow direction [Rogers *et al.* (2014), Eberle and Porcar (2012), López-Barrón *et al.* (2014)]. These microstructural rearrangements can be quantified by a scalar alignment factor [Walker and Wagner (1996)], calculated from the 2-D SANS patterns in a particular plane. The resulting anisotropy is quantified by the observed degree of increased intensity, in the q^{-1} (rod-like segment) scattering regime:

$$A_f = \frac{\int_0^{2\pi} I(q,\phi)\cos(2(\phi-\phi_0))\,\mathrm{d}\phi}{\int_0^{2\pi} I(q,\phi)\,\mathrm{d}\phi} \tag{2}$$

where I(q) is the intensity over a small fixed q-range and ϕ is the azimuthal angle and ϕ_0 is the azimuthal angle of maximum intensity.

Note that in the case of 1-3 plane rheo-SANS, $\phi_0 = 0$ due to the symmetry imposed by the method. The intensity distribution, I(q), is a projection of the material orientation distribution function (ODF) onto a particular scattering plane [Burger *et al.* (2010)]. The benefit of using the alignment factor as opposed to another orientation parameter is that the underlying material intensity distribution can be directly used to calculate the microstructural rearrangements and subsequent degree of anisotropy. Often calculations of the Hermans' orientation parameter require the intensity distribution, or orientation distribution function, to be assumed or fit to a particular model before the parameter can be derived and calculated [Burger *et al.* (2010)]. In micelles with varying topologies, a single orientation distribution, such as the commonly used Maier-Saupe potential for nematic liquid crystals [Walker and Wagner (1996), Maier and Saupe (1958, 1959)], may not be adequate to describe all systems.

Figure 6 shows the scattering and alignment as a function of shear rate for the 0.01% and 0.10% wt NaTos samples. The aligned 2-D scattering patterns vary significantly between the two samples due to the presence of the interaction peak in the 0.01% wt NaTos sample. Figure 6 specifically emphasizes the 1-3 plane alignment factor and stress at shear rates within the flow curves where the samples exhibit a high degree of shear thinning. Despite differences in the steady-shear rheology between the samples, the alignment factors follow the same trend with increasing shear rate. The high salt sample has consistently lower values of the alignment factor until the viscosity upturn (shear thickening) is encountered. This trend is also observed in samples with higher salt content [Rogers *et al.* (2014)], where the alignment factor is lower at the same absolute shear rate than that of the low salt WLMs, until a critical shear rate is reached where the alignment factor for all WLM solutions collapses onto the same curve. Here, the alignment is independent of viscosity, stress, shear rate, and sample.

To explore the shear thickening behavior of the high salt solution further, two points of roughly equal alignment between the two solutions are highlighted in Figure 6. The first set of points examined correspond to shear rates in the shear banding or shear thinning regime, while the second set correspond to rates greater than that of the observed shear thickening response. In the first pair of alignment factors, where $A_f \approx 0.3$, the nominal shear rates for equal alignment differ, as $\dot{\gamma}_{\text{low salt}} = 45$ s^{-1} and $\dot{\gamma}_{\text{high salt}} = 90$ s^{-1}. As shear thickening occurs, the alignment factors approach the same value with increasing shear rate ($A_f \approx 0.55$), as shown by the the second pair of alignment factors ($\dot{\gamma}_{\text{low salt}} = \dot{\gamma}_{\text{high salt}} = 420$ s^{-1}). Figure 7 shows the orientation distribution function and the 1-D scattering of the low and high salt samples at these two points of equal alignment. The intensity distributions are normalized to provide a fair comparison of the samples. Sector-averaged scattering was performed in the anisotropy (vorticity) direction to determine the structure of the material aligning in the flow direction, which is common practice when analyzing anisotropic or flow-aligned scattering data [Helgeson *et al.* (2009b), Weigandt *et al.* (2011)]. In highly aligned samples, there is little to no scattering along the flow axis above background so the sector-average method focuses only on the aligned material. Because the intensity distribution is a projection of the overall material orientation, any changes to the intensity distribution result from changes to the ODF and the underlying material structure.

Figure 7a shows the intensity distribution of the low and high salt samples at $\dot{\gamma} = 45$ s^{-1} and $\dot{\gamma} = 90$ s^{-1}, respectively ($A_f \approx 0.3$). Despite having the same alignment factor values, the intensity distribution of the low salt sample is much sharper than that of the high salt sample, reflecting different underlying orientation distribution functions. The sector-averaged scattering in the vorticity direction (Figure 7b) for both the low and high salt sample yields nearly identical scattering to its static structure. The change in the absolute intensity between the static and shear-induced structures results from the sector average method, where a larger fraction of the material is in the flow direction under shear as compared to the sample at rest, leading to a higher absolute intensity.

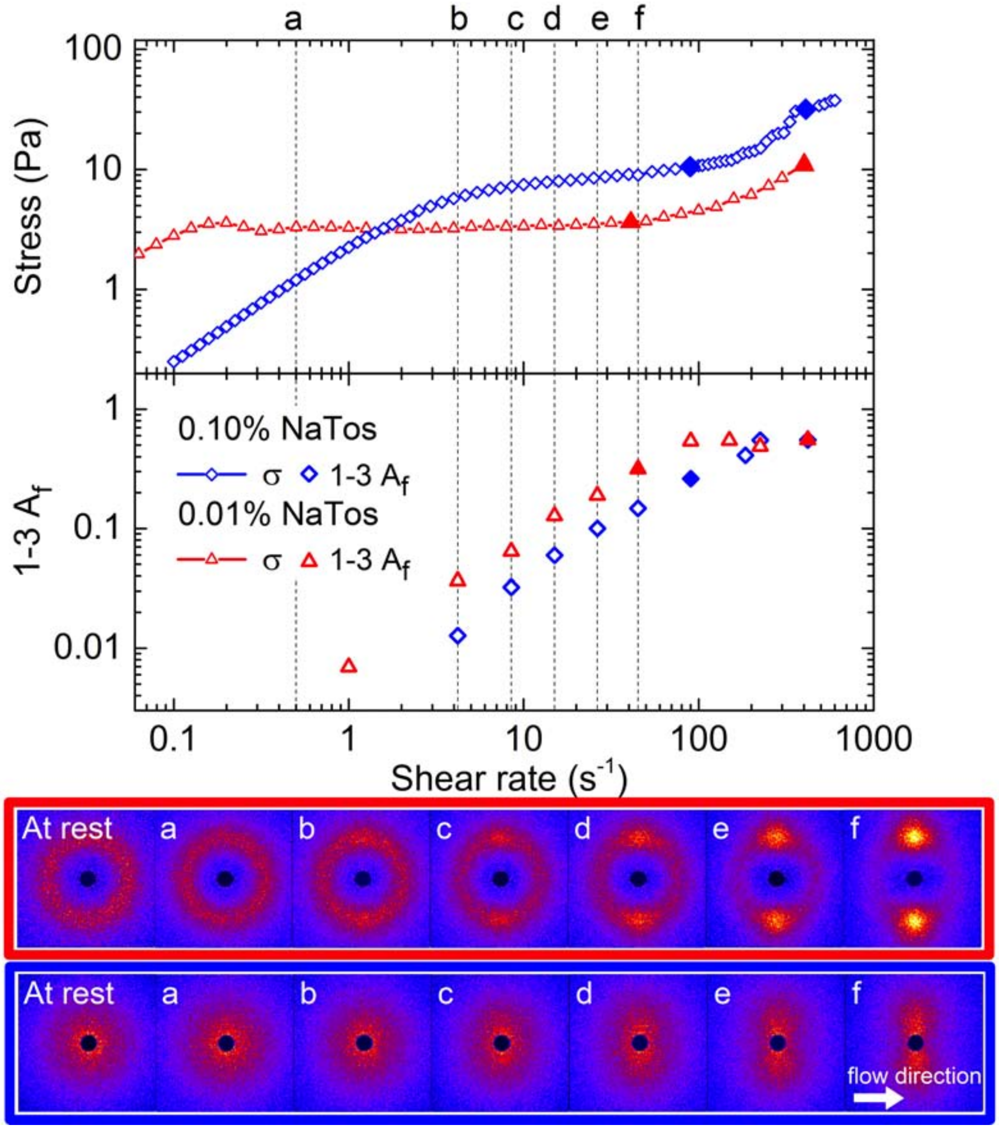

Figure 6: Alignment factor and 1-3 plane rheo-SANS scattering patterns of the low (0.01% wt NaTos) and high salt (0.10% wt NaTos) solutions at multiple shear rates across the steady shear flow curve. The mechanism of anisotropy clearly differs between the two series of scattering patterns due to the presence of the interaction peak in the low salt sample (red) and its absence in the high salt sample (blue). Resulting alignment factors are lower in the high salt case until the viscosity upturn. Two points of equal alignment between the systems are highlighted to be discussed further: one before and one after the viscosity upturn in the high salt solution.

Between Figure 7a and c, clear differences in the intensity distribution and the 1-D sector-averaged scattering are observed in the high salt sample after the onset of shear thickening. When $\dot{\gamma} = 420$ s^{-1}, both samples have the same alignment factor ($A_f \approx 0.55$) and nearly identical normalized intensity distributions. The shape of the intensity distribution with angle remains the same for the low salt case, and is the same at all shear rates for this sample, resulting from a similar underlying ODF and material structure. Conversely, the intensity distribution for the high salt sample greatly sharpens from its original form, indicative of a change in structure. At shear rates higher than the shear thickening onset, a similar ODF is observed in the high salt sample as in the low salt sample (Figure 7c). A change in structure is also detected in the 1-D sector-averaged SANS (Figure 7d), where the peak at $q = 0.022$ Å^{-1} that is not present in the high salt sample under static conditions now appears at high shear rates. In the direction of anisotropy, the structure of the high salt sample is now similar to the static structure of the low salt sample, and is quite dissimilar to its own static structure. Interestingly, the first shear rate at which this peak appears in the scattering is at the onset of shear thickening ($\dot{\gamma} = 185$ s^{-1}); thus the rheological shear thickening can be linked to a change in the SANS structure of the high salt sample. Note that there are no permanent changes to the material structure, which reverts to its static form upon the cessation of shear.

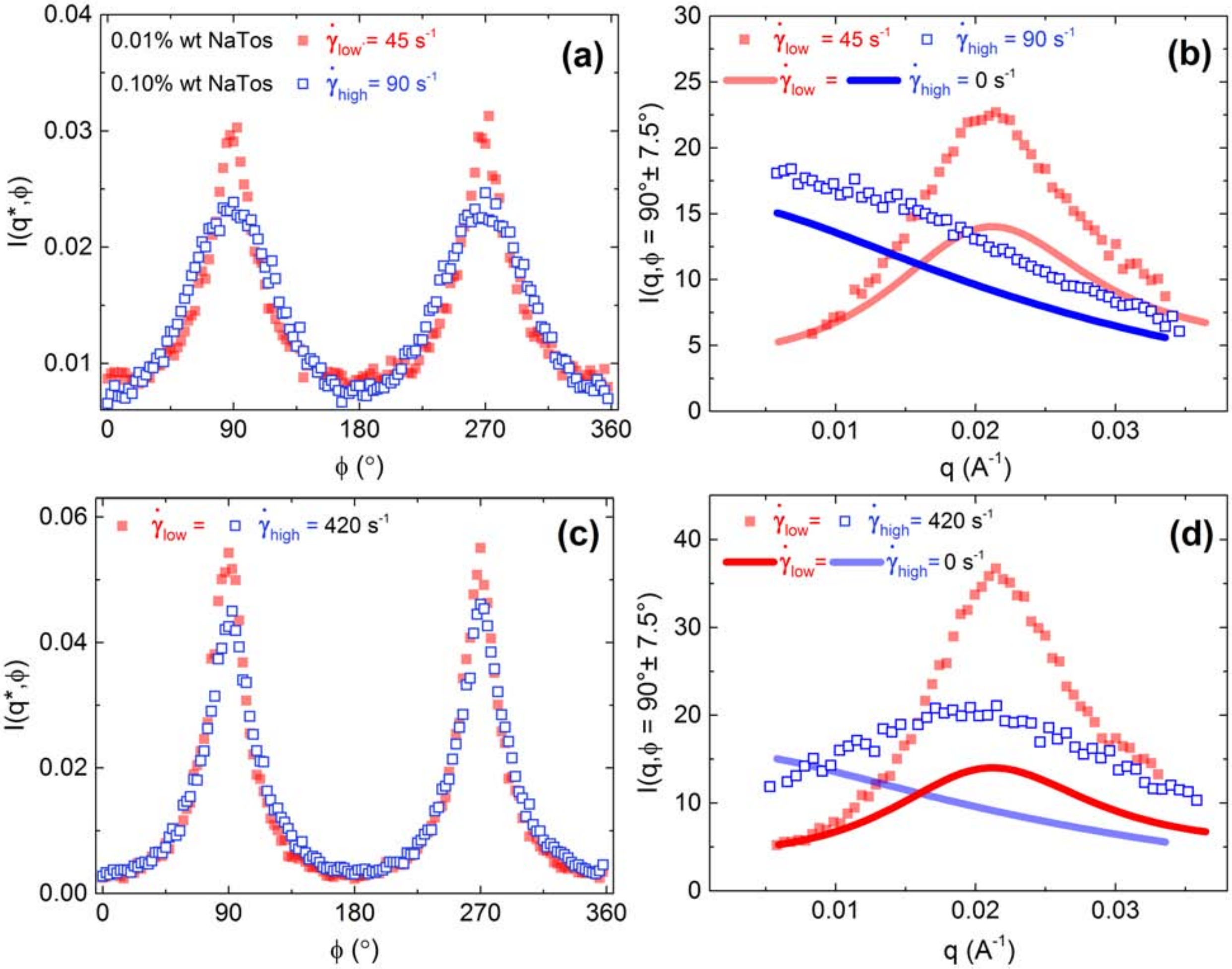

Figure 7: Normalized intensity distribution (a,c) and sector-averaged 1-D SANS in the anisotropy direction (b,d) for the low and high salt samples before (a,b) and after shear thickening (c,d), corresponding to the bolded points from Figure 6. (a) For the same alignment factor, the intensity distribution of the low salt sample is much sharper than the high salt sample, reflecting the micellar orientation and topology. (B) The SANS structure for the high salt sample under shear is nearly identical to the static high salt structure (blue line). (c) Both samples have the same alignment factor and nearly identical intensity distributions. This structural change is detected in the 1-D SANS (d), where the sector average scattering from the high salt system under strong flow is nearly identical to that of the low salt system (red line). In contrast, the structure for the low salt system under shear shows increased flow alignment but the correlation peak maintains its position with increasing rate.

We note that the 1-3 alignment factor can only provide SANS information that is convolved in space (across the Couette gap) as a function of the shear rate. When the alignment factor for the low salt sample is compared to the stress within the stress plateau, it is observed that the alignment factor increases steadily as the shear rate increases, despite the nearly constant stress. This likely corresponds with an increasing alignment and proportion of material within the high shear rate band with increasing shear rate. However, as the trends between the two systems are fairly similar, to truly resolve the nature of the material structure and flow properties across the gap, 1-2 plane structural measurements are necessary to gain spatial resolution.

2. 1-2 plane flow-SANS

Spatially-resolved, 1-2 plane flow-SANS measurements were performed at identical shear rates in order to distinguish spatially-dependent flow properties including shear banding. Measurements were taken at applied shear rates of 15, 26.4 and 45 s^{-1}, which represent three shear rates within the stress plateau (low salt) or stress gradient (high salt) regions of the flow curves. Figure 8 displays the alignment and scattering patterns at an applied shear rate of $\dot{\gamma} = 45$ s^{-1} for five positions across the gap taken with a narrow, straight slit (0.1 mm). The alignment factor for $\dot{\gamma} = 26.4$ s^{-1} and $\dot{\gamma} = 15$ s^{-1} are also shown at three gap positions. Additional measurements were taken on the 0.01% NaTos sample using a wider, 0.3 mm slit ($\diamond$) at the Institut Laue-Langevin, and a different configuration at NIST ($\bigtriangledown$) to demonstrate the versatility and reliability of the method.

The alignment for the low salt sample (red) shows interesting features suggestive of shear banding that are absent in the high salt sample (blue). As seen in Figure 8 (left), at r/H $\geq$ 0.5 in the low salt solution, all of the alignment factors and respective scattering patterns appear identical for each shear rate. This “alignment banding,” evidenced by the constant alignment in the outer portion of the gap, is strongly suggestive of shear banding. In the low shear band, it is expected that the micelles are entangled and will align little within the band. The 2-D scattering patterns shown below the figure at $\dot{\gamma}$ = 45 s^{-1} also support the shear banding thesis, as these patterns do not change in the outer half of the gap. Consequently, the underlying intensity distribution which is used to calculate the alignment factor is identical in all three measurements. As the intensity distribution is a projection of the orientation distribution function of the material and changes based on the material microstructure, these measurements indicate that the same structure is present in the outer half of the gap. This alignment banding also implies the absence of shear thinning within the low shear band, which agrees with the PIV measurements of Helgeson *et al.* (2009b) that indicate little change in material structure across the low shear band for a related system.

Conversely, the behavior of the high salt sample (blue) exhibits a gradual decrease in alignment as a function of gap position. A weak, continuous gradient in alignment is evident in the 2-D scattering patterns, where the sample becomes nearly isotropic close to the outer wall. This behavior is expected from a material that exhibits continuous shear thinning, as the decreasing shear rate with increasing gap position should correspond to a lower degree of segmental alignment with increasing gap position in such materials. The results also agree with visual observations from Helgeson *et al.* (2009a) comparing shear banding and non-shear banding solutions. In their work, there was a significant change in alignment and visual scattering from the inner to the outer wall in the shear banding CTAB sample, in accordance with the scattering from our low salt sample. However, the non-banding CTAB sample showed little difference in the scattering across the gap, in agreement with the scattering from our high salt solution. The 1-3 alignment factor for each sample at each of the three shear rates is noted with the “$\times$” symbol in Figure 8. While often (incorrectly) assumed that the 1-3 alignment factor represents an “average” alignment across the gap, the 1-3 alignment factor here is clearly below the average for the 1-2 plane alignment. Any inference that could be made about the gap behavior from the 1-3 plane alignment factor would fail to identify differences between the two samples due to their similar 1-3 plane alignment trends. The 1-2 plane SANS data, however, show strong evidence to support the shear banding and shear thinning in the low and high salt WLM systems, respectively.

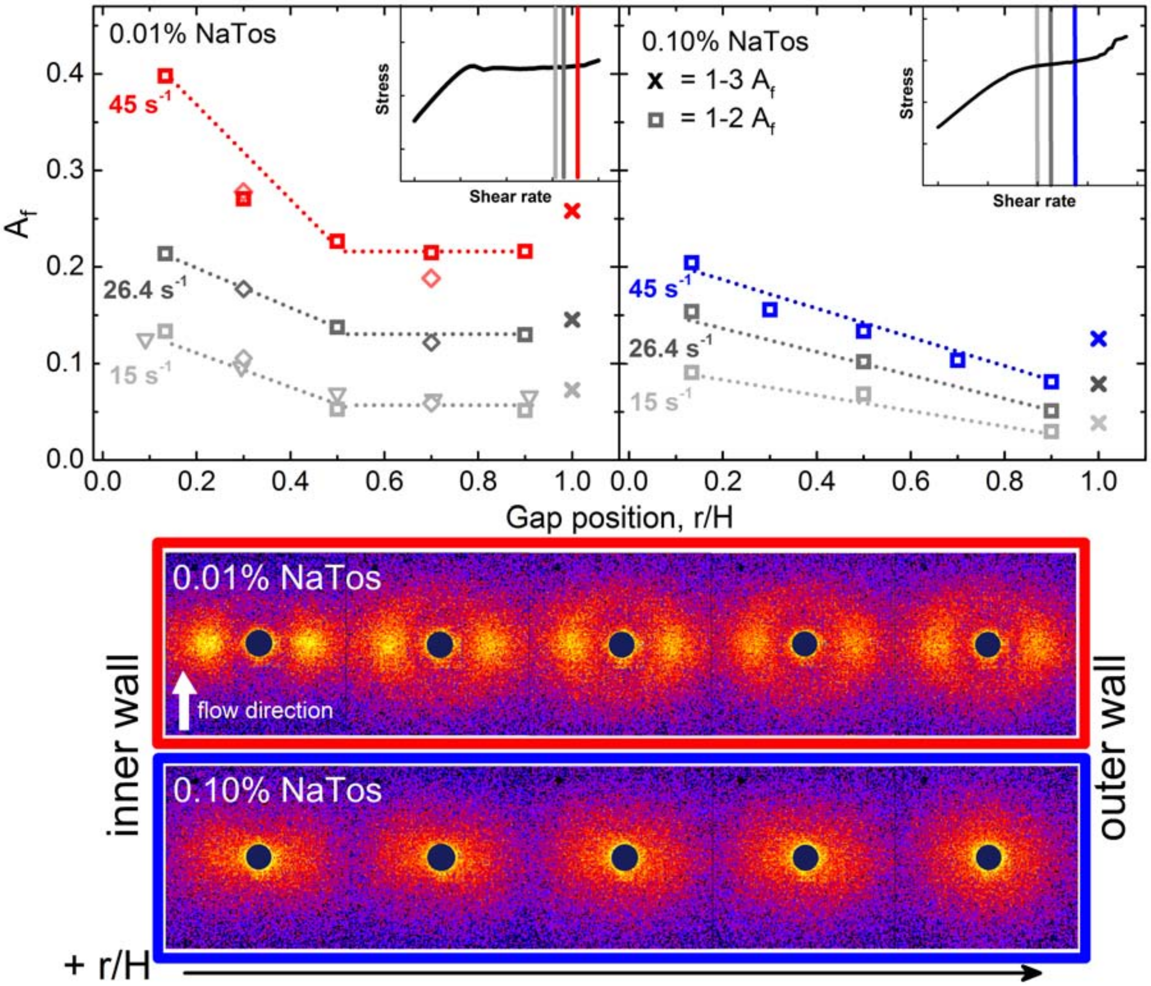

Figure 8: Alignment factor and 1-2 plane flow-SANS scattering patterns at applied shear rates of 45, 26.4 and $15\ \mathrm{s}^{-1}$ of the low salt (0.01% wt NaTos) and high salt (0.10% wt NaTos) solutions. The $\square$ symbols represent the primary set of experiments from the NIST Center for Neutron Research using a 0.1 mm fine slit, whereas the $\bigtriangledown$ and $\diamond$ symbols represent two sets of experiments using a 0.1 mm slit at NIST and a 0.3 mm curved slit at the Institut Laue-Langevin, respectively. The insets show the flow curve and the relative location of the three shear rates. The mechanism of shear banding is supported in the low salt system, as observed by a constant value of the alignment at r/H $\geq$ 0.5 at the three shear rates. Conversely, the 1-2 plane alignment provides evidence of shear thinning only in the high salt system, as the alignment continually decreases across the gap at the three shear rates. The equivalent 1-3 plane alignment factor is shown by the $\times$ symbols. Dotted lines are for visual aid only.

V. DISCUSSION

A. Salt effect on WLM topology, steady shear and LVE rheology

Topological changes observed in the cryo-TEM in addition to the rheological changes observed with added salt strongly suggest that branching is induced as hydrotropic salt is added, as concluded by Schubert *et al.* (2003). The cryo-TEM micrographs show the presence of branch points in the higher salt solutions, whereas no branch points are observed in the images of the low salt solution. The observed deviations from Maxwellian behavior at high frequency in the LVE rheology with added salt can also be attributed to branching, and such deviations are often observed in branched polymers [Burchard (1999)]. The induction of branching with added hydrotropic salt is in agreement with many other works on branched micelles using similar surfactant systems [Schubert *et al.* (2003), Sachsenheimer *et al.* (2014), Rogers *et al.* (2014)] and is often used to explain the decrease in relaxation time and zero shear viscosity with increasing salt concentration in WLMs. The presence of branched structures also helps to explain differences in the orientation distribution function (ODF) and mechanism of alignment between the low and high salt samples under shear.

As expected from Schubert *et al.* (2003), the WLM zero-shear viscosities are monotonically decreasing functions of salt concentration between 0% wt NaTos and 0.25% wt NaTos, confirming that the samples in this work are at or beyond the viscosity maximum observed for increasing surfactant concentrations. With increasing salt, branch density increases, which reduces the effective micellar contour length controlling reptation and provides additional stress relief mechanisms, thereby decreasing the relaxation time. By reducing both the breakage and reptation times, the zero-shear viscosity also decreases. As such, the branches may hinder shear thinning, as evidenced by the increase in the power law index of the 0 and 0.01% wt NaTos samples of N = 0 to N = 0.7 for the 0.25% wt NaTos sample. This may also help to explain why micellar alignment decreases with increasing branching, as linear chains may easily separate and stratify, while branches provide physical barriers to flow alignment.

In contrast to deviations in the LVE rheology attributed to branching in polymers [Burchard (1999)], the low frequency LVE for the WLMs is qualitatively similar between branching (salt) levels. This observation is in accordance with the arguments presented by Granek and Cates (1992) regarding the stress relaxation mechanisms in the fast-breaking limit, where a micelle need only reptate a small fraction of its tube because the tube is constantly breaking and reforming. The low frequency data are therefore subject to many more breakage and recombination events than are the high frequency data, leading to a single Maxwellian relaxation time. For the Maxwell model $\eta_0 = G_{\mathrm{N}}^0 \tau_R$, so the nearly constant ratio of η_0/τ_R across samples suggests the modulus remains fairly constant, which is reasonable given that the surfactant content is constant across all samples. Experimentally, G_{N}^0 is roughly equivalent for samples at low salt content, with deviations at higher levels of branching (high salt) where WLM behavior is no longer Maxwellian. Despite significant deviations from Maxwellian behavior at high salt concentration, the modulus values G_{N}^0 and G''_{min} (based on model fits) were not greatly increased by branching between the low (0.01% wt NaTos) and high (0.10% wt NaTos) salt samples. Similarly, Figure 9 shows that the crossover modulus, G_c, is relatively insensitive to added salt (branching) until $C_s > 0.15\%$ wt NaTos. The increase in G_c at higher salt concentrations can be explained by the development of connected network-like structures. In addition to providing relevant length and time scales, the LVE data can also be used to predict the first normal stress difference, N_1, in the low frequency and shear rate regimes using Laun's rule. By taking additional SANS measurements in the low shear rate regime, the stress-SANS rule [Helgeson *et al.* (2009b)] and Laun's rule can potentially be used to differentiate between branching levels by linking the micellar alignment to the expected stress response and normal stress differences.

While strictly applicable to linear, nonionic systems, the scaling laws and estimated length and time scales presented in Table 1 provide a reasonable estimate for comparing the two samples with different levels of branching. As expected from the increasing scission energy with added salt, the contour length of the branched system (high salt) was significantly higher than that of the mainly linear system (low salt). However, the reptation time decreases because the "effective length" of the branched micelles becomes the distance between

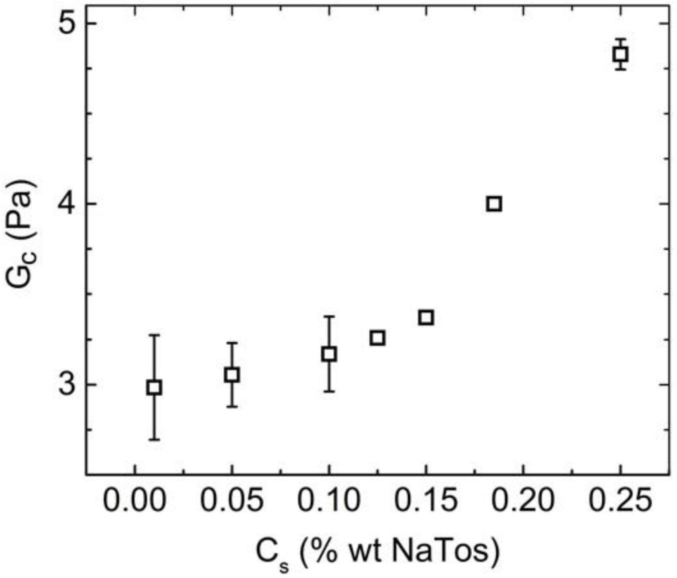

Figure 9: Crossover modulus, G_c, as a function of salt concentration (branching level). Error bars are calculated for samples with multiple preparations. G_c is more sensitive to sample preparation than η_0 or τ_R. The crossover modulus significantly increases when network-like structures become prevalent.

branch points, which is probabilistically expected to decrease with increasing salt concentration. Fitting the SANS cylinder model gives a reasonable estimate of the micelle persistence length for both samples when compared to rheo-optical measurements employed by Schubert *et al.* (2003); however, these values should be viewed with caution as fitting was performed past the interaction peak only and the fits are extrapolated to q-values below those measured.

B. Salt effect on SANS

To further address the interpretation of 1-3 plane rheo-SANS data, we revisit the flow curves and alignment factors in Figure 10, shown now on a Weissenberg number scale. Despite the differences in the steady state flow curves between the two samples with different levels of branching, similar trends are observed for the 1-3 plane alignment factors. In Figure 10, both samples show a nearly linear region of alignment as a function of Weissenberg number (or shear rate). The derivative of the alignment factor with respect to shear rate is higher in the 0.01% wt NaTos sample, whereas the derivative of the alignment factor with respect to Weissenberg number is higher in the 0.10% wt NaTos sample. Quantitatively, this results in a higher stress-SANS coefficient (analog to the stress-optical coefficient) in the branched solution (high salt) than in the linear solution (low salt) because the 1-3 plane and 1-2 plane alignment for the branched solution is lower than for the linear solution while the resulting stress is higher. The 1-3 plane SANS results indicate that branching inhibits flow alignment on a scale of absolute shear rate, whereas the opposite trend is observed based on Weissenberg number.

While both samples show a linear increase in the 1-3 plane alignment with increasing shear rate, the alignment results from different mechanisms. In the high salt sample, the alignment increases in the shear thinning region. For the low salt sample to show the same alignment trend during shear banding, the material in the high shear band must be continuously evolving toward an increasingly aligned, or nematic-like state with increasing shear rate. Furthermore, the linearity of the fit to the alignment data with increasing shear rate implies that the relative width of the bands should increase linearly with shear rate, in agreement with many recent results [Liberatore *et al.* (2006), Helgeson *et al.* (2009b), Lerouge and Berret (2010)]. With the small change in shear rate, and therefore small expected change in band width, and the limited number of 1-2 plane gap positions measured, the change in width of the bands cannot be quantified by the SANS measurements. Interestingly, the rheo-SANS alignment factor is proportional to the 1-2 plane inner wall alignment factor (r/H = 0.13) for the three shear rates investigated in the 1-2 plane experiments. However, the relationship is not a simple proportion or linear function when the rheo-SANS A_f in the low salt solution is correlated to the average 1-2 A_f across all five gap positions. This relationship can be further explained by examining the intensity distribution from the 1-3 plane SANS, which is a projection of the overall orientation distribution function (ODF) of the material onto the 1-3 plane [Burger *et al.* (2010)]. The 1-3 plane ODF is a convolution in space of several gap-dependent ODFs, and thus achieves the same maximum intensity as the 1-2 plane inner wall ODF, which masks contributions from less aligned states with lower intensities. The lower aligned states raise the background in the 1-3 plane ODF, leading to lower alignment. With increasing rate, the background rises slightly while the maximum intensity rises greatly, leading to a near proportionality between the 1-3 A_f and 1-2 plane inner wall A_f.

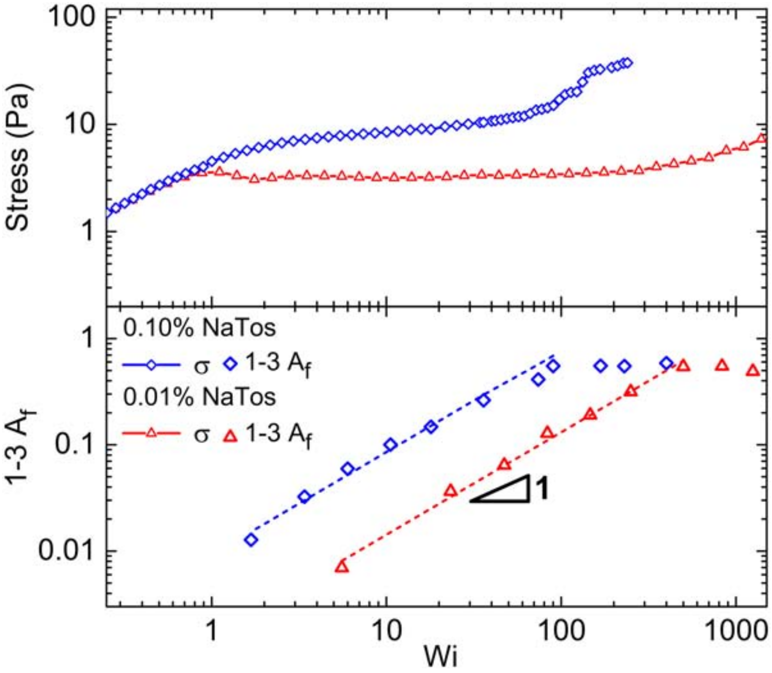

Figure 10: 1-3 alignment factor and stress of the low salt (0.01% wt NaTos) and high salt (0.10% wt NaTos) solutions on a Weissenberg number scale. Both samples show nearly linear increases in alignment with increasing Wi or shear rate.

The comparison of the 1-3 plane and 1-2 plane data, and the strong correlation between the 1-3 plane data and the 1-2 plane alignment factor at the inner wall, provides important insight into the three-dimensional structure of branched WLMs under flow. As previously mentioned, the 1-3 plane alignment factor does not represent an average alignment across the velocity gradient, as observed in Figure 8, suggesting that the micellar ODF is not uniaxial. Furthermore, both samples displayed highly similar alignment trends under 1-3 plane SANS, indicating that analyzing the 1-3 plane data alone may provide potentially misleading information. While the 1-3 plane alignment factor failed to identify differences in the gap behavior, the 1-2 plane data shows strong evidence to support the different mechanisms of shear thinning and shear banding in the low and highly branched WLM systems, respectively. Because the two samples share 1-3 plane alignment trends, no information about the flow behavior across the gap can be accurately inferred from the 1-3 plane data. The conclusions drawn from the 1-3 and 1-2 plane data highlight the importance of spatially-dependent information for confirmation of flow properties, as opposed to deducing the properties via 1-3 plane measurements.

Lastly, we examine the effect of viscosity on the alignment factor, to ensure that the observed alignment trends are a result of the topological differences in the micellar solutions. Figure 11 shows the 1-3 plane alignment factor as a function of the measured viscosity between the low and high salt solutions. In Figure

11, the results are shown for the specific samples used in this study, performed on NIST NG-3 with a large Couette geometry (R_1 = 24.0 mm, Γ = 36, ε = 0.042). In Figure 11b, results are shown from follow-up tests using new samples, on the NGB-10 instrument, with a smaller Couette geometry (R_1 = 13.5 mm, Γ = 36, ε = 0.074). Despite differences in sample batch, beamline, and geometry, the trends are nearly identical between the trials, giving further confidence in the method. Figure 11 shows clearly that at the same viscosity, the two solutions align to different degrees until a maximum alignment is reached. At a critical shear rate (as shown in Figures 6 and 10), the alignment becomes independent of viscosity, shear rate, and stress. As the microstructural rearrangements show a different and complex dependence on shear rate, stress, and viscosity between the two samples, the alignment is greatly affected by topological differences.

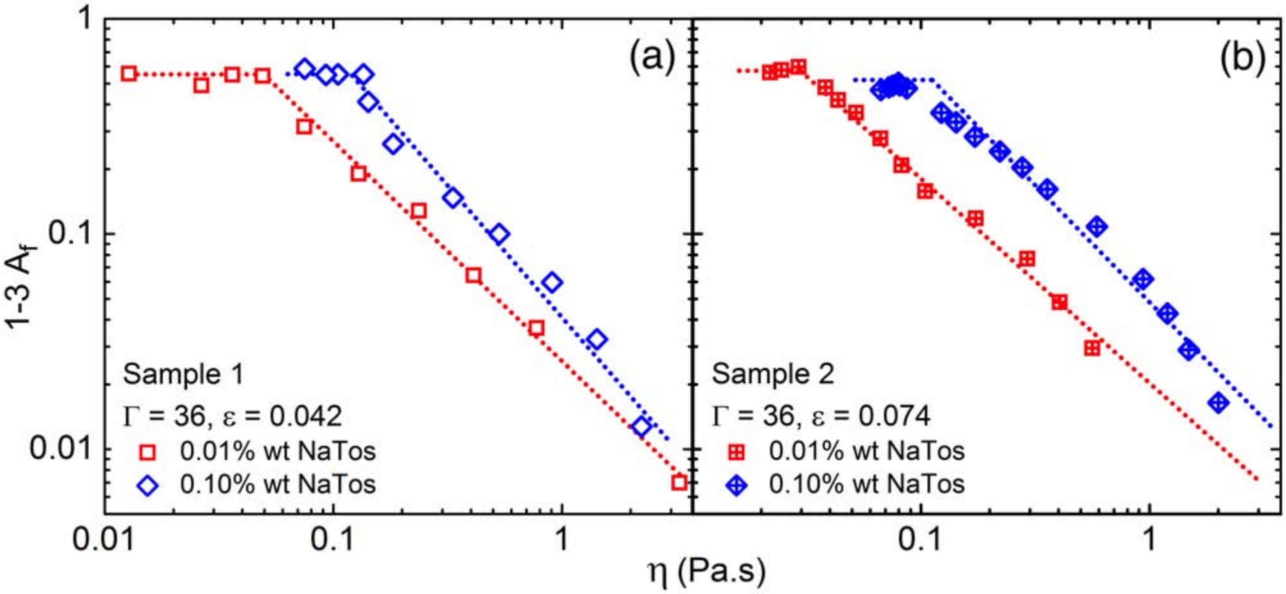

Figure 11: Alignment as a function of viscosity for the low and high salt samples in different sample preparations, geometries, and beamlines. Dotted lines are for visual aid only. (a) Results for samples reported in this study, on NIST NG-3. (b) Follow up experiments performed on NIST NGB-10. The different alignment measured for samples of the same viscosity strongly suggests that the topological differences lead to the observed alignment trends. At a critical shear rate, the alignment becomes independent of solution viscosity.

C. Interpretation of 1-2 plane SANS results

A recent review by Lerouge and Berret (2010) details the structural transitions and instabilities that are commonly observed in WLM solutions. The time- and spatially-dependent nature of such flow instabilities must be considered when interpreting the 1-2 and 1-3 plane SANS results. In the 0.01% wt NaTos, the power law index of N = 0 indicates shear banding, and the plateau spans a wide range of Weissenberg numbers, ranging from Wi = 1 to Wi ≈ 300. As noted by Lerouge and Berret (2010), shear banding flow can be geometry-dependent and also can be affected by Taylor-like vortices and elastic instabilities at high Weissenberg and elastic Taylor numbers. Such instabilities are often localized within the high shear band and the onset occurs at a critical Taylor number (see Supporting Information for calculations). As seen in Figure 11, the structural and viscosity results in the low salt solution appear to be independent of a nearly two-fold increase in ε, and the resulting flow curves are independent of geometry, suggesting that the shear banding is relatively insensitive to geometry. Furthermore, selected tests in the 1-2 shear cell were repeated on two additional occasions (Figure 8), yielding similar results. Therefore, the time-averaged structure and alignment in the shear banded state are highly repeatable in the low salt solution. However, due to the limited spatial resolution of the 1-2 plane SANS (slit size

= 0.1 mm), few gap positions measured (5), and time-averaging of the SANS data, we cannot detect specific instabilities during shear banding, such as interface fluctuations, vortices, or turbulent bursts within the high shear band. Regardless of the possible instabilities at play, the highly reproducible time-averaged scattering gives confidence in the interpretation of the SANS results that indicate shear banding in the low salt solution. One technique that can be used in the future to resolve such flow instabilities is the simultaneous rheometry and ultrafast ultrasonic imaging detailed by several recent works [Fardin *et al.* (2010), Lerouge and Berret (2010), Perge *et al.* (2014)], which will provide complementary information to the SANS results.

In the 0.10% wt NaTos solution, N = 0.15 indicates shear thinning. We note that Adams and Olmsted (2009) have shown that it is possible for models of entangled polymers to display shear banding without exhibiting a true stress plateau. However, as the surfactant concentration in these WLM solutions is low (C_D = 1.5% wt) and on the border of the dilute and semi-dilute regime ($C^* \approx$1.5% wt), it is unlikely for the high salt sample to shear band while exhibiting a positive sloping constitutive equation. Only in solutions well within the semi-dilute or concentrated regimes would this be expected [Lerouge and Berret (2010)]. Further, the maximum elastic Taylor number, Ta, reached in the 1-2 shear cell for this sample is less than 3.5, well below the critical Ta_c for elastic instability [Larson *et al.* (1994)], giving confidence in the shear thinning interpretation of the 1-2 shear cell results for the high salt solution. Additional details can be found in the Supporting Information, along with considerations of other macroscopic instabilities.

D. High salt solution - shear thickening structural transition

Shear thickening at high shear rates is commonly observed in WLM solutions, and is often attributed to a structural transition and/or elastic turbulence [Lerouge and Berret (2010), Fardin *et al.* (2010, 2014)]. Shear thickening that leads to a highly aligned or birefringent shear-induced structure is well-documented in WLM solutions in the dilute regime or near the overlap concentration ($C_D \leq C^*$) [Lerouge and Berret (2010)]. Elastic turbulence, resulting in a transition to a bi-stable state followed by fully turbulent flow, has been associated with semi-dilute WLM solutions ($C_D \gg C^*$) that are 10-fold more concentrated than the present system. Recently, Fardin *et al.* (2014) showed that in very dilute WLM solutions, the structural transition occured alongside elastic turbulence. The following rheological results, along with the structural changes observed in the 1-3 plane SANS in the shear thickening regime of the high salt solution (Figure 7), suggest that a structural transition occurs in this regime resulting in a highly ordered, anisotropic state.

1. Rheology

In this particular system (CTAT/SDBS, 97/3 weight ratio), shear thickening has been observed at similar concentrations (C_D = 0.5% wt) near $\dot{\gamma}$ = 100 s^{-1} [Koehler *et al.* (2000)], which was attributed to a structural transition. Koehler *et al.* (2000) note that the shear thickening is common at surfactant concentrations near C^*, which is the surfactant concentration used here ($C^* \approx C_D$ = 1.5% wt). As the shear thinning behavior begins at higher rates with increasing surfactant concentration [Koehler *et al.* (2000)] and the critical rate of shear thickening increases with concentration in systems of pure CTAT in D_2O [Lerouge and Berret (2010)], it is expected that shear thickening from a structural transition would also occur at C_D=1.5% wt, at $\dot{\gamma}$ >100 s^{-1}. Furthermore, the high salt solution exhibits its maximum alignment in the shear thickening regime, suggestive of a strong degree of structural order. The shear thickening response observed in the high salt sample is reproducible over different sample preparations and rheometer configurations. Figure 12 shows the similarity in the flow curves between two different sample preparations (a) and two rheometer configurations (b). The onset of shear thickening is seemingly independent of configurational changes that affect the critical inertial and elastic Taylor numbers for elastic turbulence. However, as Fardin *et al.* (2014) have shown that shear induced structure formation can occur together with elastic turbulence in dilute WLM solutions, elastic turbulence alongside the structural transition in the high salt solution cannot be ruled out. Conversely, inertial instabilities are extremely unlikely in all of the conditions studied (see Supporting Information).

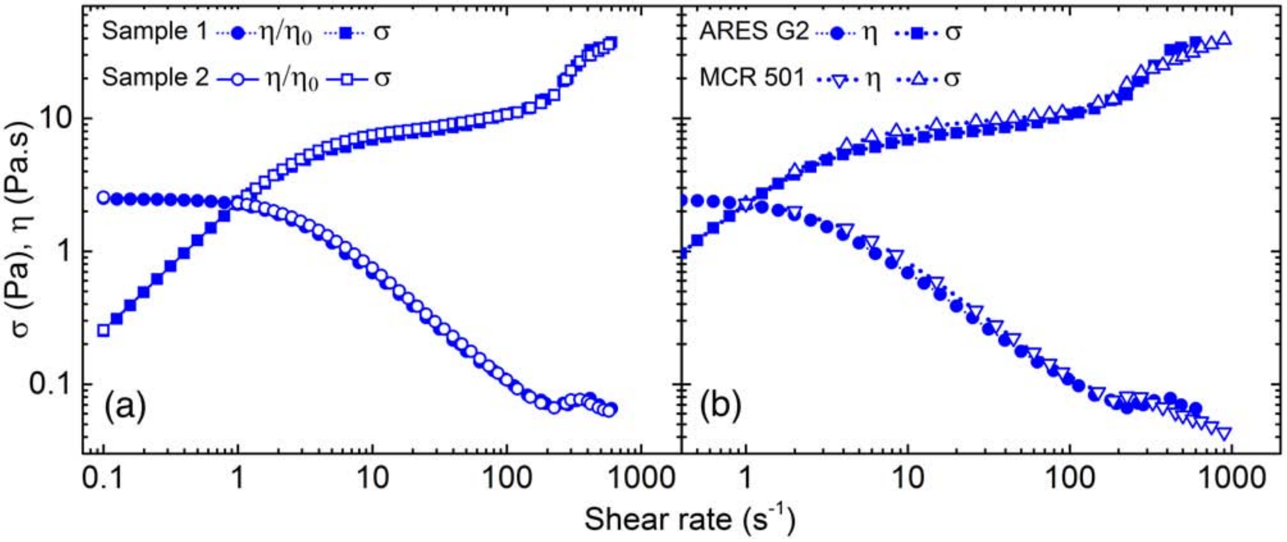

Figure 12: Repeatability of shear-thickening response of the 0.10% wt NaTos high salt WLM solution over multiple geometries and sample preparations. (a) Flow curve comparison between two sample preparations. Despite separate sample batches, the samples are nearly identical across the entire flow curve, including the shear thickening response. The original flow curve (solid points, 1) was determined by a standard sweep up test, whereas the second sample flow curve (open points, 2) was determined by long-time startup measurements. (b) Flow curve comparison between ARES G2 and MCR 501 used at NIST for SANS measurements. The shear thickening response is preserved despite differences in geometry, instrument, and sample.

The elastic Taylor number at the onset of shear thickening in the high salt sample was calculated for the geometries used in this work (see Supporting Information). The range of resulting Taylor numbers is between $12 \leq Ta \leq 20$. For comparison, in other shear thinning WLMs (N = 0.45) where both inertia and elasticity are important, the onset of inertioelastic instability occurs at an elastic $Ta_c = 22$ [Perge *et al.* (2014)]. The elastic Ta_c = 22 is greater than that expected by the Upper Convected Maxwell model ($Ta_c \approx 6$), but agrees well with predictions that take shear thinning into account [Larson *et al.* (1994)]. Using the rheological properties of the high salt solution (N = 0.85), Larson *et al.* (1994) predicts Ta_c is orders of magnitude higher than is encountered during shear thickening (see Supporting Information); however, no experimental results on very highly shear thinning WLMs are available to verify this result. Regardless, at Ta_c = 33, Perge *et al.* (2014) saw only small deviations from the base flow (δv = 0.06), indicating that if turbulence is present at the shear thickening onset, only minor deviations from the base flow would be expected. Another characteristic observed when shear thickening is accompanied by elastic turbulence is a substantial change in the level of fluctuations in the steady shear stress response in time. Recent work by Fardin *et al.* (2010) shows that for a 10-fold more concentrated, shear banding CTAB/NaNO$_3$ system in the semi-dilute regime, the stress fluctuations in the laminar flow region immediately preceding the turbulent transition are on the order of 3%, whereas in the thickening "bi-stable" regime, these fluctuations grow as high as 30%. Finally, in the fully turbulent regime, the fluctuations settle to around 15% but are still significantly larger than those observed in the laminar regime. Near the shear thickening regime in the high salt solution, long-time startup tests were performed in both the ARES G2 and the MCR 501. Unlike in the CTAB/NaNO$_3$ system, the fluctuations in the stress response at the shear rates surrounding the shear thickening regime do not change significantly with shear rate, and are on the order of 3.5% or less (see Supporting Information). Because shear thinning increases the Ta_c for elastic turbulence, the shear thickening is not dependent on geometry, and the stress fluctuations are minor, we believe that the structural transition occurs without significant elastic turbulence or deviations from the base flow. However, due to limited previous work on non-shear banding, highly shear thinning WLMs, we cannot rule out more substantial contributions to the shear thickening from elastic turbulence. Regardless, the interpretation of our results in the context of a shear thickening structural transition would not change, as Fardin *et al.* (2014) has shown that such a transition to a highly-ordered, anisotropic state and elastic turbulence can occur together. Additional details and calculations can be seen in the Supporting Information.

2. 1-3 plane SANS

As mentioned previously, shear thickening is also observed in samples with higher degrees of branching (higher NaTos concentrations). We believe that this shear thickening structural transition corresponds to the point at which branches begin to break, leading to an alignment of highly ordered linear chains. As the steric hindrance to alignment is removed when branches break, the aligned chains should obtain the maximum degree of alignment at and beyond these shear rates. Fittingly, A_f remains constant with increasing shear rate after this proposed breakage point, which is observed in Figures 6 and 10. Figure 7 provides further evidence to support this notion of branch breakage, as clear changes to the orientation distribution function and the SANS structure of the high salt sample occur after the shear thickening onset. Branch breakage should lead to alignment of linear chains and similar ODF between the two samples, which is the result observed in Figure 7.

The differences in the ODFs between the two samples can be explained by topological differences. Before the shear thickening region, the intensity distribution of the low salt (low branching) sample is much sharper than the high salt (high branching) sample, even when the alignment is equal. In the low salt sample, the alignment results from only linear chains, leading to a sharp, narrow Poisson-like ODF. Conversely, in the high salt sample, the “backbones” of the chains may align, but the many branches and junctions may extend outwards from the main chain, resulting in a wider distribution that is well-described by the Maier-Saupe distribution. The branched structures flow with the “backbones” and therefore do not align perfectly in the flow direction. The alignment factor in the highly branched case therefore has contributions to the $\cos(2\phi)$ term from many partially aligned branches, whereas the low branched structure has contributions from primarily fully flow-aligned chains. This difference in mechanism of alignment enables the branched structure to have the same value of alignment from a less steep orientation distribution. While the shape of the intensity distribution remains constant for the low salt case at all shear rates studied, the intensity distribution for the high salt sample changes in the shear thickening region, indicative of changing structure that may result from branch breakage. Fittingly, at shear rates higher than the shear thickening onset, a similar structure and ODF is observed in the high salt sample as in the low salt sample. Similar phenomena are observed in samples with higher levels of salt (branching), with SANS structural changes directly corresponding with shear thickening in the steady-shear flow curve [Rogers *et al.* (2014)]. The shear rate at which shear thickening is observed increases with branching level. If branch breakage contributes to the structural transition, this would be expected due to the faster breakage time that results from increasing salt content (Table 1).

The observed changes in the material orientation distribution function emphasize the importance of using several metrics when quantifying anisotropy in flow-induced structures. A metric such as the alignment factor that makes no assumptions about the underlying ODF is helpful to describe the overall alignment, as the ODF is shear rate-dependent. However, examining the shape of the ODF provides additional insight into the alignment mechanism and material structure. By utilizing the ODF in the analysis of anisotropy, we gain information that is otherwise lost by the use of a single order parameter. The ODF analysis paired with the sector averaged SANS confirms that the material structure changes at the shear rates surrounding shear thickening, supporting a structural transition from branch breakage.

VI. CONCLUSIONS

Branching was induced to varying degrees in a model series of worm-like micelles via the addition of a hydrotropic salt, as confirmed by a combination of cryo-TEM, rheology, and small angle neutron scattering under flow. At the surfactant concentration studied, the zero-shear viscosity and relaxation time of samples as a function of salt content, and therefore branching, decrease monotonically, in agreement with the results of Schubert *et al.* (2003) (Figure 3). Linear rheological behavior becomes increasingly non-Maxwellian as the salt content is increased, and high rate shear thickening results from a structural transition (Figures 4 and 5). A new method of analyzing the effects of branching in worm-like micelles and possible branch breakage has been proposed using the scattering intensity distribution, or orientation distribution function (ODF). Examining the ODF provides more information about the underlying material structure than alignment factor analysis alone. The widening of the micellar ODF under flow with increasing salt concentration supports increasing branch density. At equal shear rates, branched micelles flow-align less than their linear counterparts, despite higher shear stresses (Figure 6). This behavior persists until a critical shear rate is reached, which is dependent on the level of added salt and branching (Figure 6). At this critical shear rate, shear thickening is observed and the ODFs of the branched micelles become comparable to those observed for the linear WLMs (Figure 7). Sector-averaged SANS under flow confirms that the micellar structure is different at rates in excess of the critical value. We have confirmed alignment banding in low salt (low branched) WLMs by the use of 1-2 plane SANS measurements at multiple positions across the gap. The results (Figure 8) verify that the shear banding phenomenon in linear WLMs is not observed when significant branching is present. A multi-technique experimental approach, combining data from linear and nonlinear rheology, SANS, and cryo-TEM, has enabled us to link micellar microstructure and topology to the macroscopic flow properties of WLM solutions, providing a more complete data set for further interpretation of the rheology and rigorous testing of microstructure-based constitutive equations.

VII. ACKNOWLEDGEMENTS

We acknowledge the W. M. Keck Microscopy Facility at the University of Delaware for the use of the cryo-TEM and Vitrobot. We also acknowledge the support of the National Institute of Standards and Technology, U.S. Department of Commerce, and the Institut Laue-Langevin in Grenoble, France in providing the neutron research facilities used in this work. This manuscript was prepared under cooperative agreement 70NANB12H239 from NIST, U.S. Department of Commerce. The statements, findings, conclusions and recommendations are those of the author(s) and do not necessarily reflect the view of NIST or the U.S. Department of Commerce.

References

Adams, J. and P. Olmsted, "Nonmonotonic models are not necessary to obtain shear banding phenomena in entangled polymer solutions," Physical Review Letters **102**, 067801 (2009).

Angelico, R., S. Amin, M. Monduzzi, S. Murgia, U. Olsson, and G. Palazzo, "Impact of branching on the viscoelasticity of wormlike reverse micelles," Soft Matter **8**, 10941–10949 (2012).

Barati, R. and J.-T. Liang, "A review of fracturing fluid systems used for hydraulic fracturing of oil and gas wells," Journal of Applied Polymer Science **131**(2014).

Berret, J. F., J. Appell, and G. Porte, "Linear rheology of entangled wormlike micelles," Langmuir **9**, 2851–2854 (1993).

Britton, M. and P. Callaghan, "Shear banding instability in wormlike micellar solutions," The European Physical Journal B-Condensed Matter and Complex Systems **7**, 237–249 (1999).

Burchard, W. (1999), Solution properties of branched macromolecules, *in* "Branched polymers II,", Springer, pp. 113–194.

Burger, C., B. S. Hsiao, and B. Chu, "Preferred orientation in polymer fiber scattering," Journal of Macromolecular Science, Part C: Polymer Reviews **50**, 91–111 (2010).

Candau, S. and R. Oda, “Linear viscoelasticity of salt-free wormlike micellar solutions,” Colloids and Surfaces A: Physicochemical and Engineering Aspects **183**, 5–14 (2001).

Cates, M. and S. Candau, “Statics and dynamics of worm-like surfactant micelles,” Journal of Physics: Condensed Matter **2**, 6869 (1990).

Cates, M. E. and S. M. Fielding, “Rheology of giant micelles,” Advances in Physics **55**, 799–879 (2006).

Cross, M. M., “Rheology of non-Newtonian fluids: a new flow equation for pseudoplastic systems,” Journal of Colloid Science **20**, 417–437 (1965).

de Gennes, P. G. (1979), *Scaling concepts in polymer physics*, Cornell University Press.

Doi, M. and S. Edwards (1986), *The theory of polymer dynamics*, Claredon, Oxford.

Drye, T. and M. Cates, “Living networks: The role of cross-links in entangled surfactant solutions,” The Journal of Chemical Physics **96**, 1367–1375 (1992).

Eberle, A. P. and L. Porcar, “Flow-SANS and rheo-SANS applied to soft matter,” Current Opinion in Colloid & Interface Science **17**, 33–43 (2012).

Fardin, M.-A., D. Lopez, J. Croso, G. Grégoire, O. Cardoso, G. McKinley, and S. Lerouge, “Elastic turbulence in shear banding wormlike micelles,” Physical Review Letters **104**, 178303 (2010).

Fardin, M., C. Perge, N. Taberlet, and S. Manneville, “Flow-induced structures versus flow instabilities,” Physical Review E **89**, 011001 (2014).

González, Y. I. and E. W. Kaler, “Cryo-TEM studies of worm-like micellar solutions,” Current Opinion in Colloid & Interface Science **10**, 256–260 (2005).

Grand, C., J. Arrault, and M. Cates, “Slow transients and metastability in wormlike micelle rheology,” Journal de Physique II **7**, 1071–1086 (1997).

Granek, R., “Dip in G$''$ of polymer melts and semidilute solutions,” Langmuir **10**, 1627–1629 (1994).

Granek, R. and M. Cates, “Stress relaxation in living polymers: results from a Poisson renewal model,” The Journal of Chemical Physics **96**, 4758–4767 (1992).

Gurnon, A. K., P. D. Godfrin, N. J. Wagner, A. P. Eberle, P. Butler, and L. Porcar, “Measuring material microstructure under flow using 1-2 plane flow-small angle neutron scattering,” JoVE (Journal of Visualized Experiments) , e51068–e51068 (2014).

Hatzikiriakos, S. G., “Long chain branching and polydispersity effects on the rheological properties of polyethylenes,” Polymer Engineering & Science **40**, 2279–2287 (2000).

Helgeson, M., M. Reichert, Y. Hu, and N. Wagner, “Relating shear banding, structure, and phase behavior in wormlike micellar solutions,” Soft Matter **5**, 3858–3869 (2009a).

Helgeson, M., P. Vasquez, E. Kaler, and N. Wagner, “Rheology and spatially resolved structure of cetyltrimethylammonium bromide wormlike micelles through the shear banding transition,” Journal of Rheology **53**, 727–756 (2009b).

Khatory, A., F. Lequeux, F. Kern, and S. Candau, “Linear and nonlinear viscoelasticity of semidilute solutions of wormlike micelles at high salt content,” Langmuir **9**, 1456–1464 (1993).

Kline, S. R., “Reduction and analysis of SANS and USANS data using IGOR Pro,” Journal of Applied Crystallography **39**, 895–900 (2006).

Koehler, R. D., S. R. Raghavan, and E. W. Kaler, “Microstructure and dynamics of wormlike micellar solutions formed by mixing cationic and anionic surfactants,” The Journal of Physical Chemistry B **104**, 11035–11044 (2000).

Koshy, P., V. Aswal, M. Venkatesh, and P. Hassan, “Unusual scaling in the rheology of branched wormlike micelles formed by cetyltrimethylammonium bromide and sodium oleate,” The Journal of Physical Chemistry B **115**, 10817–10825 (2011).

Kuperkar, K., L. Abezgauz, D. Danino, G. Verma, P. Hassan, V. Aswal, D. Varade, and P. Bahadur, “Viscoelastic micellar water/CTAB/NaNO3 solutions: Rheology, SANS and cryo-TEM analysis,” Journal of Colloid & Interface Science **323**, 403–409 (2008).

Larson, R., S. Muller, and E. Shaqfeh, “The effect of fluid rheology on the elastic Taylor-Couette instability,” Journal of Non-Newtonian Fluid Mechanics **51**, 195–225 (1994).

Lequeux, F., “Reptation of connected wormlike micelles,” Europhysics Letters **19**, 675 (1992).

Lerouge, S. and J.-F. Berret (2010), Shear-induced transitions and instabilities in surfactant wormlike micelles, *in* “Polymer Characterization,”, Springer, pp. 1–71.

Liberatore, M. W., F. Nettesheim, N. J. Wagner, and L. Porcar, “Spatially resolved small-angle neutron scattering in the 1-2 plane: A study of shear-induced phase-separating wormlike micelles,” Physical Review E **73**, 020504 (2006).

Liberatore, M. W., F. Nettesheim, P. A. Vasquez, M. E. Helgeson, N. J. Wagner, E. W. Kaler, L. P. Cook, L. Porcar, and Y. T. Hu, “Microstructure and shear rheology of entangled wormlike micelles in solution,” Journal of Rheology **53**, 441–458 (2009).

López-Barrón, C. R., A. K. Gurnon, A. P. Eberle, L. Porcar, and N. J. Wagner, “Microstructural evolution of a model, shear-banding micellar solution during shear startup and cessation,” Physical Review E **89**, 042301 (2014).

Lopez-Barron, C. R. and N. J. Wagner, “Solvent isotope effect on the microstructure and rheology of cationic worm-like micelles near the isotropic-nematic transition,” Soft Matter **7**, 10856–10863 (2011).

Lu, T., L. Xia, X. Wang, A. Wang, and T. Zhang, “A dually effective inorganic salt at inducing obvious viscoelastic behavior of both cationic and anionic surfactant solutions,” Langmuir **27**, 9815–9822 (2011).

MacKintosh, F., S. Safran, and P. Pincus, “Self-assembly of linear aggregates: the effect of electrostatics on growth,” Europhysics Letters **12**, 697 (1990).

Magid, L., “The surfactant-polyelectrolyte analogy,” The Journal of Physical Chemistry B **102**, 4064–4074 (1998).

Maier, W. and A. Saupe, “Eine einfache molekulare theorie des nematischen kristallinflüssigen zustandes,” Zeitschrift Naturforschung Teil A **13**, 564 (1958).

Maier, W. and A. Saupe, “Eine einfache molekularstatistische theorie der nematischen kristallinflüssigen phase. teil i,” Zeitschrift Naturforschung Teil A **14**, 882 (1959).

Maitland, G., “Oil and gas production,” Current Opinion in Colloid & Interface Science **5**, 301–311 (2000).

Oelschlaeger, C., M. Schopferer, F. Scheffold, and N. Willenbacher, “Linear-to-branched micelles transition: a rheometry and diffusing wave spectroscopy (DWS) study,” Langmuir **25**, 716–723 (2008).

Palazzo, G., “Wormlike reverse micelles,” Soft Matter **9**, 10668–10677 (2013).

Perge, C., M.-A. Fardin, and S. Manneville, “Inertio-elastic instability of non shear-banding wormlike micelles,” Soft Matter **10**, 1450–1454 (2014).

Porcar, L., D. Pozzo, G. Langenbucher, J. Moyer, and P. Butler, “Rheo-small-angle neutron scattering at the National Institute of Standards and Technology center for neutron research,” Review of Scientific Instruments **82**, 083902 (2011).

Rogers, S. A., M. A. Calabrese, and N. J. Wagner, “Rheology of branched wormlike micelles,” Current Opinion in Colloid & Interface Science (2014).

Sachsenheimer, D., C. Oelschlaeger, S. Müller, J. Küstner, S. Bindgen, and N. Willenbacher, “Elongational deformation of wormlike micellar solutions,” Journal of Rheology **58**, 2017–2042 (2014).

Schubert, B. A., E. W. Kaler, and N. J. Wagner, “The microstructure and rheology of mixed cationic/anionic wormlike micelles,” Langmuir **19**, 4079–4089 (2003).

Schubert, B. A., N. J. Wagner, E. W. Kaler, and S. R. Raghavan, “Shear-induced phase separation in solutions of wormlike micelles,” Langmuir **20**, 3564–3573 (2004).

Shrestha, R. G., L. Abezgauz, D. Danino, K. Sakai, H. Sakai, and M. Abe, “Structure and dynamics of poly (oxyethylene) cholesteryl ether wormlike micelles: Rheometry, SAXS, and cryo-TEM studies,” Langmuir **27**, 12877–12883 (2011).

Spenley, N., M. Cates, and T. McLeish, “Nonlinear rheology of wormlike micelles,” Physical Review Letters **71**, 939 (1993).

Thareja, P., I. H. Hoffmann, M. W. Liberatore, M. E. Helgeson, Y. T. Hu, M. Gradzielski, and N. J. Wagner, “Shear-induced phase separation (SIPS) with shear banding in solutions of cationic surfactant and salt,” Journal of Rheology **55**, 1375–1397 (2011).

Walker, L. M., “Scattering from polymer-like micelles,” Current Opinion in Colloid & Interface Science **14**, 451–454 (2009).

Walker, L. M. and N. J. Wagner, “SANS analysis of the molecular order in poly (γ-benzyl l-glutamate)/deuterated dimethylformamide (PBLG/d-DMF) under shear and during relaxation,” Macromolecules **29**, 2298–2301 (1996).

Weigandt, K. M., L. Porcar, and D. C. Pozzo, “In situ neutron scattering study of structural transitions in fibrin networks under shear deformation,” Soft Matter **7**, 9992–10000 (2011).

Yang, J., “Viscoelastic wormlike micelles and their applications,” Current Opinion in Colloid & Interface Science **7**, 276–281 (2002).

Zakin, J. L., B. Lu, and H.-W. Bewersdorff, “Surfactant drag reduction,” Reviews in Chemical Engineering **14**, 253–320 (1998).

Ziserman, L., L. Abezgauz, O. Ramon, S. R. Raghavan, and D. Danino, “Origins of the viscosity peak in wormlike micellar solutions. 1. mixed catanionic surfactants. a cryo-transmission electron microscopy study,” Langmuir **25**, 10483–10489 (2009).